Experimental model of plug formation in subsea pipelines

Vegar Hovdenakk Øye

Master's Thesis
Ocean Technology - Marine installations
Department of Physics and Technology
University of Bergen

June 1, 2022

Acknowledgements

Foremost, I would like to express my greatest appreciation to my supervising associates, Boris V. Balakin of the Department of Mechanical and Marine Engineering, Western Norway University of Applied Sciences, as well as Pawel Kosinski of the Department of Physics and Technology, University of Bergen. Thank you Boris for your passionate involvement with the project, guidance, encouragement and discussions throughout the project. Thank you Pawel Kosinski for your passionate involvement as well as valuable inputs during meetings. You have both been very helpful for me during this period. The entire Flowchart group also deserves a valuable mention as throughout the project different calculations, simulations and valuables could be investigated by a larger group of researchers, and discussed during meetings.

A special thanks to Pavel G. Struchalin of the Department of Mechanical and Marine Engineering, Western Norway University of Applied Sciences, for your incredible work ethic and intellect. With all the flow loop experiments we conducted together discussions were endless, and a deeper understanding of every problem we encountered was easier obtained. Thank you Pavel for all the insightful comments and discussions.

I would also show my gratitude to Alex C. Hoffman for contributing during the experiments, and discussions regarding the packing limit factor calculations obtained in these experiments. I would also like to thank all the mechanical engineers at Western Norway University of Applied Sciences workshop, where help with fittings, electrical schemes, LabView programming is amongst many problems they could provide helpful insight in.

Finally I will thank both the University of Bergen and Western Norway University of Applied Sciences for this opportunity to contribute with the work submitted. The learning curve has been steep at times, but the knowledge I have learnt will never disappear.

Vegar Hovdenakk Øye
Bergen, June 2022

Abstract

Slurries of cohesive particles constitute a significant risk during subsea petroleum production due to their potential to plug the flow. This thesis investigates the plug formation of a slurry mixture with 0.23 mm ice particles in continuous phase decane. The experimental study was conducted with particle volume concentrations up to 20.3 %, and Re<25000. The cohesion forces of the ice particles were controlled by controlling the temperature of the slurry flow. The relative viscosity of the slurry was computed as a function of particle concentration using pressure drop measurements of the flow loop system. The relative viscosity was 3.2 for the concentration of 20.3 %. The Bingham-fluid model agreed with the empirical data, and the slurry showed shear-thinning tendencies. The test section of the loop was equipped with an orifice to induce the formation of plugs. The plugging of the flow loop was observed at particle concentrations below 7.0 %. In this thesis, detailed experimental logs are depicted, showing the changing of the particle sizes and circularity through flow loop experiments. The observed blocking cases were partially agreed with the literature, and a risk evaluator for plug formation is presented. The particle drop measurements will further be used in investigations associated with tracing a labeled particle in a flow regime where the plug is formed.

Contents

Acknowledgements i

Abstract iii

1 Introduction 1
1.1 Motivation . . . 1
1.2 Specific objects . . . 2

2 Theoretical analysis and background 3
2.1 Literature review . . . 3
2.2 Multiphase flow and fluid rheology . . . 5
2.2.1 Newtonian and non-Newtonian fluid . . . 7
2.2.2 Total pressure loss . . . 8
2.2.3 Ice slurry properties . . . 9
2.2.4 Particle forces . . . 10
2.2.5 Thermal properties of slurry . . . 10

3 Methods 13
3.1 Experimental methods . . . 13
3.1.1 Experimental procedure in the flow loop experiments . . . 13
3.1.2 Slurry preperation . . . 17
3.1.3 Rheological analysis . . . 18
3.2 Particle size measurement . . . 19
3.3 Particle drop-tests . . . 20

4 Results and Discussion 23
4.1 Overview of experiments . . . 23
4.2 Flow loop pressure drop readings . . . 24
4.2.1 Flow map- risk evaluator . . . 27
4.2.2 Summary . . . 29
4.3 Particle size distributions from the samples . . . 30
4.3.1 Manual count of particles . . . 30
4.3.2 Average diameter and circularity . . . 34
4.3.3 Change in diameter through flow loop experiments . . . 34
4.3.4 Ice particle's properties . . . 38
4.3.5 Summary . . . 38
4.4 Particle drop test velocities . . . 39

5 Conclusions and future work **43**
5.1 Conclusion 43
5.2 PEPT-experiments for particle tracking 44

Supplementary materials **49**
5.2.1 Computing viscosity from the pressure drop data 49
5.2.2 Particle drop test 54
5.2.3 Water quality 55

Nomenclature

α	Volume fraction
$\bar{\rho}$	Bulk density
$\dot{\gamma}$	Shear rate
$\dot{V}_x$	Volumetric flow rate of x-phase
η	Apparent viscosity
λ	Thermal conductivity
μ	Dynamic viscosity
ψ	Mean circularity
ρ	Density
σ_s	Strength of agglomerate
τ	Shear stress
ξ	Flow resistance coefficient
A	Area
c, ϕ	Concentration
c_p	Specific heat capacity
D	Diameter
fr	Fractal dimension
g	Gravitational acceleration
l	Characteristic length
m	Mass
P	Pressure
R_e	Reynolds number
T	Temperature

t	Time
U_m	Mean flow velocity
v, u	Velocity
V	Volume
x, y, z	Distance

List of Figures

2.1 Schematic drawing of flow classification in general flow theory. 5
2.2 Phase inversion of water-oil interaction. 6
2.3 Illustrative rheogram to define Newtonian slurries, adapted from *Crowe*. 7
2.4 Graphical representation of four major slurry-transport flow regimes, gathered from *Baha Abulnaga* (2021). 8

3.1 The hydraulic scheme of the flow loop. P, T, F denote pressure, temperature and flow rate measurements. 14
3.2 Schematic model of the flow-loop. 15
3.3 Model of the set-up made for photoes of the particles taken from slurry. 20
3.4 Schematic model of the model for drop test experiments. 21

4.1 Absolute (A) and relative (B) total pressure drop in the ice slurry flow (between "P" pressure sensor and the expansion tank). 25
4.2 Relative viscosity of ice slurry. 26
4.3 Blockage risk evaluator. 29
4.4 Ice particles. 31
4.5 Projected area of particles. 31
4.6 Outlines of particles. 32
4.7 Frequency distribution of particle size's compared. 32
4.8 Average D_p of volume concentration slurry mixtures. 36
4.9 Average circularity of volume concentration slurry mixtures. 37
4.10 Particles (A), and projected area (B). 39
4.11 Absolute velocity. 40
4.12 Rolling velocity 40

5.1 Settling time velocities of ice particles dropped in subcooled decane. . 54
5.2 Chemical composition water. 55

Chapter 1

Introduction

1.1 Motivation

When studying at NTNU - Trondheim, my field of research was oil- and gas technology. In this study, background knowledge of the mechanics within the petroleum industry was obtained, and the solution to most common problems was often in question. One of these subjects was the course "Subsea technology", where subsea pipelines were the main focus. Through various meetings with operators, and employees of energy companies such as Lundin Norway AS, Equinor, and Aker BP, it was clear that the petroleum industry is fighting towards a more environmentally green industry, and the question of the MEG injection was often brought up. MEG (Mono-ethylene glycol) is a chemical introduced to the flow to mitigate plug formation in subsea pipelines. The chemical is not wanted in the crude oil and has to be separated at large industrial plants before the crude oil can further be used for its purposes. The cost of these injections is like everything in the petroleum industry, relatively expensive, and solutions to prevent MEG injection were wanted in the industry.

In the petroleum industry today, chemicals are used to mitigate the formation of hydrate and wax plugs in subsea lines. Subsea pipelines can reach several kilometers from the oil field to the shore, etc. where the multiphase flow is further separated and treated at large industrial plants like the Mongstad refinery. The chemicals introduced to the flow alter the cohesion of the hydrates so that a plug is not formed in the pipelines. The investigation of plug formation at large dimensions is not the most common research, as the cost of operating would vastly exceed the risk of the experiment's success. However, slurry experiments at lower dimensional sizes are quite common, as the understanding of multiphase flow is a desired practice since energy often is transported in pipeline systems.

The physics behind plug formation is highly dependent on the cohesion of the particles, and in the petroleum industry the most problematic slurries in question are the gas hydrates, waxes and their mixtures *Sloan* (2010) *Geest et al.* (2021). To obtain a higher understanding of plug formation physics, a more detailed study has to be conducted. *Hirochi et al.* (2002) further investigated the plugging in ice slurries in an experimental

flow loop system, where a flow restriction was inserted into the pipe to induce a plug.

The project hypothesized that if the system is investigated dimensionless, a risk evaluator for plug formation can be obtained, accurately predicting the plugging of the flow loop system. Therefore, the cohesion of the particles, flow regime, temperature, particle size as well as volume concentration had to be controlled within the experiments. This project will contribute to the fundamental understanding of the influence of dimensionless flow parameters with an experimental approach of plugging pipes with adhesive particles.

1.2 Specific objects

The specific objectives for this thesis was to:

- Design and assistance in the construction of the experimental flow loop.
- Calculate the hydraulic losses of the flow loop.
- Obtain a control for the hydraulic resistance of the flow loop experimentally.
- Investigate the slurry properties
- Conduct flow experiments, altering flow parameters: temperature, flow rate and concentration.
- Develop a model for PEPT-experiment to study particle interactions.

Chapter 2

Theoretical analysis and background

This chapter presents the theoretical background which is necessary for the experimental procedures to be validated. First, the literature review is presented, where background knowledge for conducting flow loop experiments is achieved. Further theoretical equations useful for understanding calculations in the project are derived.

In the first section of theoretical equations, an introduction to basic fluid mechanics is presented. The following section follows up on the interactions between the particles, constituted in the fluid.

2.1 Literature review

To investigate the plugging of a subsea-pipeline system with a slurry mixture, there have been different methods presented in the literature. *Majid et al.* (2018) investigated the flow and formation of a methane slurry in a flow loop filled with a three-phase mixture of crude oil, brine and methane. In their research a 4-inch flow loop was used, and they recorded a remarkable elevated pressure drop when more than 15% of the hydrates where formed in the slurry, mainly when the oil content was high. Other researches of slurry-flow experiments include *Vijayamohan et al.* (2014), who studied a 3-inch flow loop, and the results were similar as of Majid. These researches utilized complex high-pressure systems, and the process of plugging were not studied in full. The parameters that were uncertain in the slurry for researching the process of plugging in detail were the particle size, cohesive force, and volume fraction of the particles.

Another approach to determine the flow loop pressure measurements is to consider the rheology of the hydrate slurries. In this method characterization of the slurry is made by combining desired parameters of the flow into yield stress and apparent viscosity. *Darbouret et al.* (2005) conducted this method with a laminar flow loop experiment using a water-based slurry of tetra-n-butylammonium bromide hydrate. This slurry was found to be a shear-thinning (Bingham) type fluid with the yield stress of 4 Pa at 50 % particle load. *Fidel-Dufour et al.* (2006) also did a similar experiment where a laminar slurry of methane hydrates was formed in a water-dodecane emulsion. The findings concluded that the apparent viscosity of the slurry depended on the mean size

of the particles, and the relative viscosity of the slurry with a particle concentration of 16 % was above 6.0. For Fidel to fit the experimental data, the rheological expression by *Snabre and Mills* (1996) was used. The difficulty of using these rheological studies is to relate the findings to an industrial case, where a turbulent regime is more likely.

Further *Ding et al.* (2019) performed a comprehensive rheological study of a natural gas hydrate slurry. In this study the particle size and pressure drop in a 25 mm flow loop was controlled. In their findings they concluded that the rheological expression by *Snabre and Mills* (1996) was a good fit to their experimental results with the emulsion-hydrate slurry. This means that hydrate-based slurries can be characterized by an effective volume fraction beyond the actual solid content in the system. In these experiments there was not reported any plugging of the system.

Research on both laminar and transitional flow regimes has also been conducted by *Beata Niezgoda-Zelasko* (2007), where the pressure drop in a flow loop was measured with a slurries of particle concentration below 30 %, and particle size's of 100-150 μm. They reported an increasing pressure drop for increasing ice concentration for both laminar and transitional regimes. They also found that the presence of the particles did not contribute to the pressure drop for the transitional flow regimes. In this experiment the pressure drop in the slurry was lower than that of a one-phase flow of the carrier liquid for the equal flow velocity. *Onokoko et al.* (2018) did an analysis of the pressure drop in a pipe flow of slurry with 20% wt ice particles, and found a low influence of the particle concentration on the pressure drop for velocities above 2 m/s. In *Beata Niezgoda-Zelasko* (2007) the pressure drops of lower velocity ($0.08 m/s$) resulted in a doubling of pressure drop decrease with ice concentration increasing from 5 % wt. to 20 % wt.

Bordet et al. (2018) conducted experiments in a straight horizontal pipe with ice slurry, with concentration up to 18.4 %, and particle size of 250 μm. In this experiment, the pressure drop and flow patterns were investigated. The result of pressure drops for the 18.4 % concentration was 1.6 times higher for 0.6 m/s, and 21.7 times higher for 0.025 m/s, both compared to the pressure drops of the pure carrier fluid at the respected velocities. In this study, there was no reported any plug of the system in the majority of the experiments with the ice particles, but the influence of $\approx$ 10 % ethanol or glycol will decrease the cohesion of the ice and is considered the reason for this.

Other experimental studies of ice slurries is *Rensing et al.* (2011), where an ice slurry in crude oil with ice concentrations up to 70 % were conducted. This slurry was produced by cooling a water-in-oil emulsion to achieve droplet sizes of below 3 μm. It was found that the slurry was shear thinning for concentrations above 10 %, and at concentration of 50 % the relative viscosity of the fluid was equal to 25. When the concentration exceeded 25 % the slurry acted as a Bingham fluid, with a yield stress present, this yield stress was in the interval of 300 to 3000 Pa. Comparing the slurry made from brine-in-oil emulsion to a pure-water ice slurry, the relative viscosity for pure-water case was at least twice higher, indicating a higher cohesion for this case.

When considering experiments on plugging in ice slurries, *Hirochi et al.* (2002) is one of a few. In this study, a flow loop with 52 mm pipeline was blocked by a water-ice slurry. The pipeline had inserted an orifice, to decrease the cross-sectional area drastically, and increase the chances of plugging in this area. The particle size of his experiment was 1 mm, with particle concentration up to 40 %. In his experiments a flow map of the process was determined, to show different flow regions, and to predict plugging for different flow velocities. In the flow map presented in his work, plug was formed at flow velocities lower than 0.12 m/s for a very thin slurry. However, when the flow velocity increased to 0.5 m/s a plug was not possible until the particle concentration increased beyond 32 %.

2.2 Multiphase flow and fluid rheology

Laminar flow and turbulent flow are the two definitive flow classifications in general flow theory. Between these two states, the flow is classified as transitional. The cross-sectional flow profiles of the laminar and turbulent regimes represent different orders of particle motion manner. In the turbulent flow, the particle motion is highly disordered, and each particle moves randomly in three different dimensions. In the laminar flow, the flow profile is more of a streamlined flow, with particle motion in an ordered manner. These differences influences the maximum flow velocity (V_{max}) of these regions, where the general order is that laminar flow has V_{max} in the center of the flow, and the lowest near the pipe wall. The maximum flow velocity for laminar flow is generally considered $V_{max} \approx 2\bar{v}$, where $\bar{v}$ is the mean flow velocity across the cross-sectional area. For the turbulent flow profile, the maximum flow velocity is considered $V_{max} \approx 1.2\bar{v}$, spreading over a larger area of the cross-section. A schematic representation of the flow classification states is shown in figure 2.1.

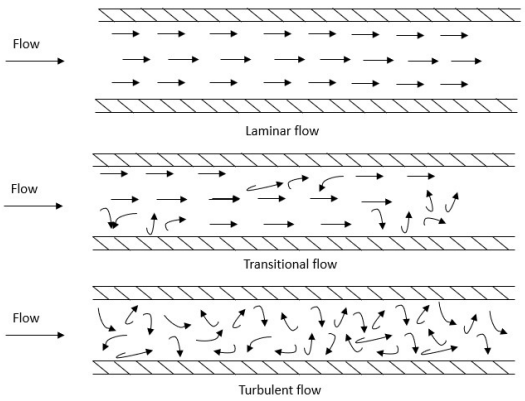

Figure 2.1: Schematic drawing of flow classification in general flow theory.

To distinguish the state of the flow, the Reynolds number, from equation 2.1 is used:

$$Re = \frac{vl\rho}{\mu} \tag{2.1}$$

where l is a characteristic length, v the flow velocity, ρ the flow density, and μ is the dynamic viscosity. The flow is further defined as laminar if the Reynolds number is below $2 \cdot 10^3$, and turbulent for $Re > 10^4$.

Multiphase flow is the flow of a system consisting of multiple thermodynamic phases and/or components. The three physical states possible are the solid, liquid, and gas states. In a solid-state, each crystalline form constitutes a separate phase. In liquid, it's normally one phase, except for helium, and gas has only one phase possible. It is also possible to have a system with one component and more phases, such as water together with ice at the freezing point of water. In immiscible fluids, the two-phase mixture will make up different phases, comparing the water-oil interaction, and the continuous- and dispersed phase. A schematic representation of this is shown in figure 2.2.

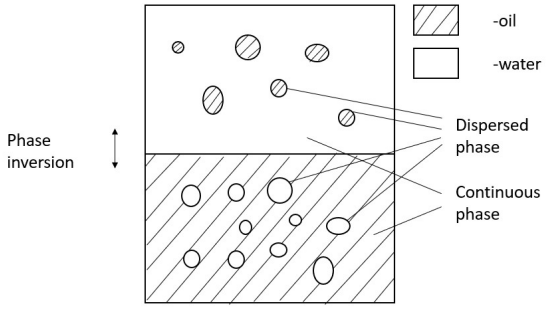

Figure 2.2: Phase inversion of water-oil interaction.

The modeling of multiphase flow strongly links to the laws of buoyancy, which was discovered by Archimedes and gave ground to the Archimedes' principle. Archimedes principle states that, as defined by *encyclopedia* (2022), "any body completely or partially submerged in a fluid (gas or liquid) at rest is acted upon by an upward, or buoyant, force, the magnitude of which is equal to the weight of the fluid displaced by the body." Archimedes' principle is defined in equation 2.2:

$$F_a = \rho g V \tag{2.2}$$

To define the velocity of a slurry flow, a mean slurry flow velocity (U_m) is defined:

$$U_m = \frac{\dot{V}_d + \dot{V}_c}{A} \tag{2.3}$$

where $\dot{V}_d$ and $\dot{V}_c$ are the volumetric flow rate of dispersed phase (solids) and continuous phase (liquid), respectively.

2.2.1 Newtonian and non-Newtonian fluid

The steady-state rheological behavior of most slurry mixtures can be expressed by the following general form*Crowe*:

$$\tau = \eta \dot{\gamma} \tag{2.4}$$

where τ is the shear stress, $\dot{\gamma}$ is the shear rate, and η is the apparent viscosity.

Newtonian fluids are by definition fluids where the viscosity of the fluid is constant for different rates of shear stress. Viscosity is the fluid's resistance to flow, and its polar opposite fluidity is a measure of ease in flow. By plotting the shear stress τ versus the shear rate $\dot{\gamma}$, a rheogram is produced. The rheogram adapted from *Crowe* is shown in figure 2.3. Where the apparent viscosity is constant and equal to the slope, the slurry has Newtonian behavior. If the slurry has a decreasing apparent viscosity to the increasing rate of shear $\dot{\gamma}$ the behavior is called pseudo-plastic, or shear thinning. Another term when investigating fluids is the Bingham fluid. This behavior will be as the shear thinning shown in the figure, where the fluid acts as a rigid body until a certain pressure (yield pressure) is applied from which the fluid will then flow as a plug. The last behavior possible is if the apparent viscosity η increases with the rate of shear $\dot{\gamma}$, and this behavior is termed dilatant or shear thickening. A schematic representation of these behaviors is shown in figure 2.3.

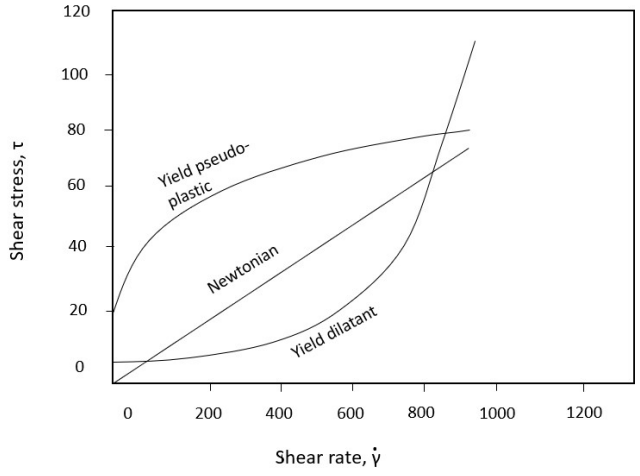

Figure 2.3: Illustrative rheogram to define Newtonian slurries, adapted from Crowe.

.

Known highly viscous fluids are for example honey or cold maple syrup, and low viscous fluids, benzene or water. Viscosity is measured in pascal-seconds and depends highly on the temperature of the medium. Dynamic, or absolute viscosity is the fluid's internal resistance to flow when a force is applied, and kinematic viscosity refers to the ratio of dynamic viscosity to its density.

Furthermore, the flowing of a system of stable and unstable flow regions of non-Newtonian slurries can be described, recommended by *Poloski et al.* (2009), depending on three correlations to the deposition boundary. The three correlations include: 1) the critical deposition boundary, 2) the transitional deposition boundary, and 3) the laminar deposition boundary. As interpreted in *Baha Abulnaga* (2021) these boundaries correspond to different physical transport of the dispersed phases, and the four major regimes are presented in figure 2.4.

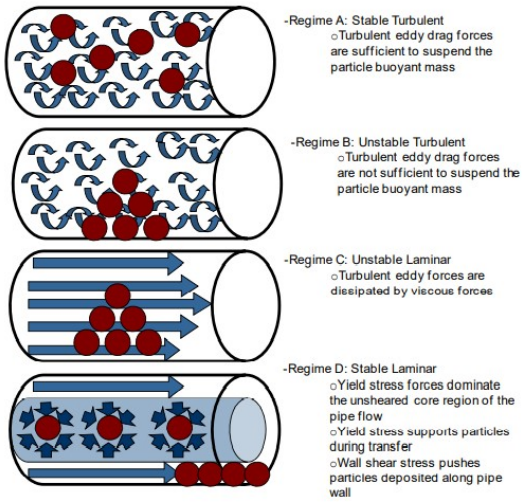

Figure 2.4: Graphical representation of four major slurry-transport flow regimes, gathered from Baha Abulnaga (2021).

.

2.2.2 Total pressure loss

The total pressure drop between the pump and expansion tank was calculated from the following equation, where the flow was assumed a homogeneous slurry.

$$\Delta p = \sum_{i=1}^{N} \lambda_i \frac{l_i}{d_i} \frac{\rho_{mix} u_i^2}{2} + \sum_{j=1}^{M} \xi_i \frac{\rho_{mix} u_j^2}{2} + \rho_{mix} g z_p, \tag{2.5}$$

where l_i and d_i are the length and the equivalent hydraulic diameter of ith pipe element on the way to the tank; u_i and u_j are the average flow velocities in the pipe element and in the jth local flow restriction (e.g., bend, orifice). Furthermore, $\rho_{mix} = \phi_p \rho_p + \rho_l (1 - \phi_p)$ is the density of the mixture with the volume fraction of particles ϕ_p with indices denoting the particles (p) and the carrier liquid (l). The hydrostatic

pressure difference is defined by the elevation of the tank z. The friction coefficients λ_i and the local flow resistance coefficients ξ_i were set dependent on the local Reynolds number Re_i. These coefficients were calculated following *Idelchik* (2008). A complete set of the used equations is available in the Supplementary materials.

2.2.3 Ice slurry properties

Defining the properties of dispersed phase flows is only possible by defining a statistically significant measure of density in a volume δV° that contains "enough particles" (e.g. 1000^b). The density of any point is defined as:

$$\rho = \lim_{\delta \to 0} \frac{\delta M}{\delta V} \tag{2.6}$$

Further mixture density is defined as:

$$\frac{\delta M}{\delta V^\circ} = \rho_m \tag{2.7}$$

Calculating volume density, or the volume fraction of the dispersed phase, for the dispersed phase α_d, where δV_d is the dispersed phase in δV is given by *Crowe*:

$$\alpha_d = \lim_{\delta V \to \delta V^\circ} \frac{\delta M_d}{\delta V} \tag{2.8}$$

For calculating the volume fraction for the continuous phase α_c, the equation is modified by changing the numerator volume to the volume δV_c of the continuous phase within the same volume ∂M. The mass density, or bulk density of the dispersed phase further is defined as:

$$\bar{\rho_d} = \lim_{\delta V \to \delta V^\circ} \frac{\delta M_d}{\delta V} \tag{2.9}$$

This density is distinct from the dispersed phase's material density, or actual density ρ_d. For this equation the same principle for calculating the continuous phase's bulk density ($\bar{\rho_c}$) of modifying follows.

Furthermore the mass density of the mixture (ρ_m), or mixture density is defined as:

$$\rho_m = \bar{\rho_d} + \bar{\rho_c} = \alpha_d \rho_d + \alpha_c \rho_c \tag{2.10}$$

2.2.4 Particle forces

Considering the particles in motion in the non-Newtonian fluid, cohesive and adhesive forces is the dominant factors of determining agglomeration of particles. In particle-fluid interactions, a general equation for the sum of forces on the particle is provided in *Crowe*:

$$m\frac{\delta v}{\delta t} = \sum F = 3\pi\nu D(u-v) + u.s.t \tag{2.11}$$

where D is the diameter of the particle in $[m]$, ν is the kinematic viscosity of the fluid $[g/mol]$, u is the superficial velocity, or the velocity of the continuous phase $[m/s]$, and v is the velocity of the dispersed phase (particle) in $[m/s]$. "u.s.t" further stands for unsteady terms, and is divided into two parts, the virtual mass effect, and the Basset-term. These forces is a case of the acceleration of the particle with respect to the carrier liquid. Virtual mass describes the forces where the mass of the fluid around the particle must be accelerated with the particle. The Basset-term describes boundary layers around the particle, where the force on the particle depends on the history of these boundary layers. The Basset-term, or "history" term is normally neglected in calculations, because of it's difficulty to implement.

In this equation submitted in the literature, the first term concludes the average force due to quasi-steady drag, and further the effects of mass transfer between the particles and the fluid were omitted, and the heat transfer from a severed particle (i.e., the boundary of a numerical cell slicing the particle) and the molecular (i.e., conduction and viscous) terms have been neglected.

2.2.5 Thermal properties of slurry

For further calculations, the thermal properties of the slurry mixture had to be determined. First, the thermal property of the carrier fluid was determined. For the density of the decane, a polynomial expression was obtained from the "webbook.nist.gov" site for fluid data when analyzing the decane in different temperature regimes.

The polynomial method for calculation was also provided for the heat capacity, thermal conductivity and dynamic viscosity of the carrier fluid.

The following equations were obtained by data obtained from the NIST webbook, for the continuous phase liquid (decane):

for density:

$$\rho_d = 746 - 0.07803 \cdot T + 8.89 \cdot 10^{-5} \cdot T^2 \tag{2.12}$$

heat capacity:

$$c_{pd} = 2104.0 + 3.362 \cdot T + 7.004 \cdot 10^{-3} \cdot T^2 \tag{2.13}$$

thermal conductivity:

$$\lambda_d = 0.01361 - 2.659 \cdot 10^{-4} \cdot T + 6.349 \cdot 10^{-8} \cdot T^2 \tag{2.14}$$

dynamic viscosity:

$$\mu_d = 0.001278 - 2.345 \cdot 10^{-5} \cdot T + 2.461 \cdot 10^{-7} \cdot T^2 \tag{2.15}$$

Further for calculating the properties of the dispersed phase, ice particles, the same method was used, where the equations are as followed:
density:

$$\rho_{ice} = 917 \cdot (1 - 1.17 \cdot 10^{-4} \cdot T) \tag{2.16}$$

heat capacity:

$$c_{ice} = 185 + 6.89 \cdot (T + 273.15) \tag{2.17}$$

thermal conductivity:

$$\lambda_{ice} = 1.16 \cdot (1.91 - 8.66 \cdot 10^{-3} \cdot T + 2.97 \cdot 10^{-5} \cdot T^2) \tag{2.18}$$

Chapter 3

Methods

In this chapter, a more detailed description of how the experiments were conducted and evaluated is derived. The experiments conclude the experimental results of pressure drops in the flow loop system, how the slurry was prepared before each experiment, a method for determining the particle sizes of the ice particles in the slurry mixture, and the method of the particle drop test measurements.

3.1 Experimental methods

In this section, the methods involving each of the three different measuring parts of this study are presented. First, the procedure carried out for the experiments with the flow loop is described, which is distinguished from the slurry preparation and particle measurement in this section. Further, the other model experiment with the PEPT-model is explained.

After the theoretical background was set, the method of achieving results was clear. For controlling the particle sizes of the slurry, sampling and picture measurements were to be made throughout the flow loop run time. For this a valve for sampling the slurry was important, but this valve will change the geometrical shape of the flow loop and has a high chance of plugging. For further investigation, a PEPT-experiment to trace a radioactive particle's movement when approaching plug formation at the orifice for certain criteria was planned, and for this, an additional injection pipe was planned close to the orifice. For this ice-ice collision measurements had to be evaluated, and a small model for ice-particle-ice-surface collision was to be made.

3.1.1 Experimental procedure in the flow loop experiments

To further develop the experimental approach proposed by *Hirochi et al.* (2002), a flow loop with a transparent test section, inserted with an orifice was to be built. In the experimental setup of Hirochi, the cohesion of the particles was estimated through a compression test, where the different ice particle sizes were $D_p = 1, 3$ and 10 mm. In

Yang et al. (2004), the particle-particle pull off adherence forces were measured as a function of temperature in the ice/n-decane/ice and tetrahydrofuran (THF) hydrate/n-decane/THF hydrate with a micro-mechanical testing technique. For this technique, the cohesion of the ice particles could be determined by the temperature interval and conditions of the flow. With this basis, the experimental design of the flow loop could be determined, avoiding complex methods by utilizing the rheological expression by *Yang et al.* (2004), further described in the later part of the methods.

The main idea that this flow loop could determine the temperature difference and pressure drops over the orifice, flow velocity, particle size, and concentration as well as control the temperature of the flow. The flow loop also had to be portable, and fit inside a standard ceiling height room. For economic purposes, the flow loop needed a loading and drainage application, so the continuous phase liquid could be reused in further experiments, after separation. The test section had to be mounted at a certain height for later experiments with a PET scanner and the piping to be inclined at a small angle ($\approx 2\,\text{deg}$) for the liquid to flow out of the flow loop. For the highest possibility of plugging, and to make the flow regime as close to a laminar flow as possible at the orifice in the test section, the piping of this part was to be maximized within the geometrical shape. A hydraulic scheme of the flow loop is shown in figure 3.1

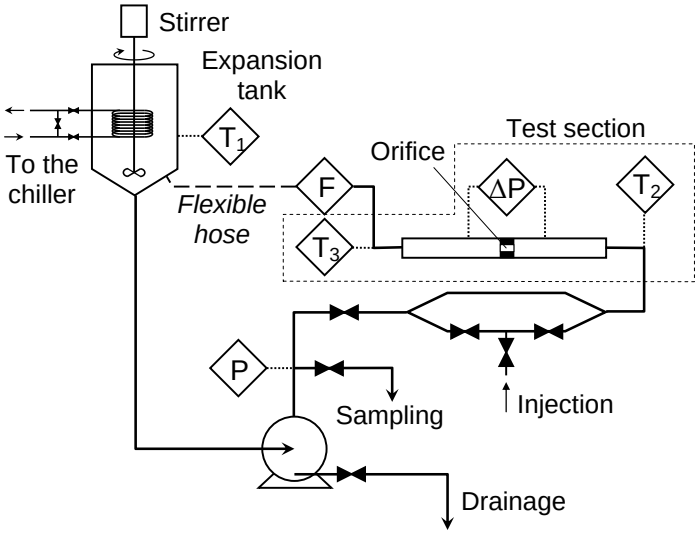

Figure 3.1: The hydraulic scheme of the flow loop. P, T, F denote pressure, temperature and flow rate measurements.

The flow loop to be constructed needed the above-mentioned criteria, an expansion tank where the liquid could be loaded into the system, a heat exchanger for temperature control, a flow meter to determine flow velocity, pressure sensors to determine the pressure drops through the flow loop, and temperature sensors to record the temperature control throughout the experiments. A schematic presentation of the flow loop constructed is shown in figure 3.2.

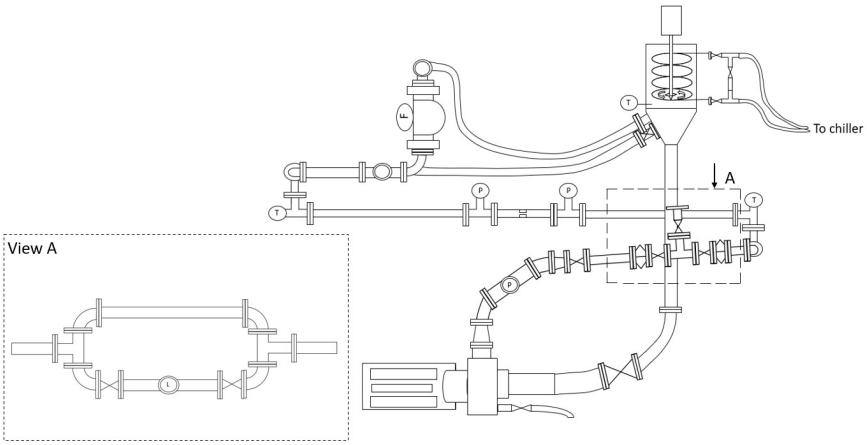

Figure 3.2: Schematic model of the flow-loop.

This system is a closed flow loop where ice slurry was pumped through a transparent test section, between the pressure sensors at the longest horizontal pipe of the system. This section was 1.73 m in length and had an inner diameter of 22 mm, with a 1.5 mm wall thickness. The walls of the tubing were made of 304 stainless steel. At the ends of the test section piping, the temperature sensors were placed in two 90-degree T-junctions to control the temperature most accurately at the orifice, without disturbing the flow state at the orifice. The orifice equipped at the test section acted as a restriction to the flow, to increase the probability of plug formation. The diameter of this restriction was 9.5 mm, and the length was 10 mm. Also, there were two facets (1 mm $\times$ 45°) in the orifice.

From the temperature sensor at the test section inlet to the orifice the distance was 85 cm, which corresponds to 38.6 hydraulic diameters. The transparent section of the system was of length 110 mm and was made of glass (borosilicate glass 3.3), and within this glass pipe, the orifice was mounted with epoxy glue. The total lengths of steel piping and flexible hoses were 6.7 m and 1.3 m, respectively. The flexible hoses enabled the test section to be tilted at desired angles when needed (draining etc.). The internal surface of the hoses was covered with smooth nitrile rubber. The flow loop included two 45° bends in the metal pipes after the pump, where a pressure sensor was placed to determine the pressure after the pump, and fourteen 90° bends in the pipes in total (including the turns inside the flow meter). In view A, a bifurcation of the pipes with an injection port is shown, because in later experiments a radioactive ice particle was to be injected into the flow tracing the particle through plug formation. This experiment is done after the criteria for plug formation are determined.

For pumping the slurry, a centrifugal pump (Pedrollo HF 70A, 2.2 kW) was placed at the lowest part of the construction, coupled with a frequency converter (ABB ACS355). The flow rate in the system was altered with the usage of the frequency converter by altering the frequency manually. The casing of the pump was made of cast iron, and the closed-type impeller was made of brass. The axial clearance in the pump was 4 mm. The impeller with seven blades had a thickness of 10 mm and a diameter of 200 mm.

The measurement system of the flow loop consisted of a digital manometer at the outlet from the pump, a differential manometer at the test section, a Coriolis mass flowmeter after the test section, and several sensors for temperature control. To determine the number of bends and internal geometry of the channels in the flow meter, computer tomography on the flow meter was made. The specifications of the sensors are presented in Table 3.1. The sensor signals were collected and processed using the National Instrument 6001 DAQ USB data card operated under a LabView-based control program with an acquisition frequency of 1 kHz.

Table 3.1: Measurement system.

Parameter	**Sensor**	**Meas. range**	**Inst. error**
Temperature	PT100 + LKM 103 Transducer	-40...85 C	$\pm$0.1 C
Pressure	Gems 3500 Pressure Transmitter	0...4 barg	0.25%
Differential pressure	Omega PXM219-006AI	0...6 bar	0.25%
Flow rate	Micro Motion Coriolis Flow Meter (R050S Sensor,1700 Transmitter)	0...3600 kg/h	0.5%

At the highest point of the flow loop, the expansion tank, made of 304 stainless steel was placed. This expansion tank was open to the atmosphere, and fitted with an overhead stirrer (Joanlab OSC-20L). The stirrer was fitted with a 75 mm three-blade impeller and was operated at 1700 rpm for each test. The impeller's function was to homogenize the slurry and prevent stagnant conditions in the large diameter of the tank to prevent unnecessary plugging conditions at this part. The tank itself was used for filling, cooling, and dispersion of the slurry. The dimensions of the expansion tank consisted of a cylindrical top part with (310 mm, 310 mm height) and a conical bottom part (35 mm bottom, 230 mm height). For this, the total volume of the expansion tank is equal to 29.9 l. The expansion tank was also equipped with an installed heat exchanger of rectangular coiling inside the tank. The coiling was connected to the chiller (WTG-Quantor Chilly 25 M-LT) for the system, which was built of stainless steel 304 metal pipes (10×1 mm). The rectangular coiling consisted of 14 coils with the dimension of 120×50 mm and a radius of 25 mm. In the figure of the flow loop, the bypass line of the coolant system is also shown, where it was possible to alter the flow rate of the coolant to change the heat transfer to the slurry. The coolant was a 35 %vol. propylene glycol - water mixture, and the head of the pump (Y 2051.0263) was 0.44 m^3/h at 3.0 bar.

The first part of the flow loop measurements, with the flow loop shown in figure 3.2, was done to establish the heating of the system without a heat exchanger to determine the possible time for loading the system with the pure continuous phase liquid and slurry before the liquid in the system became too heated. In this part, both a pure liquid of 25 l of ethanol with a purity of 99>%, also applied from the Sigma Aldrich company,

as well as the pure decane when subcooled to -22.3 °C were loaded into the system. When the loading was completed, the pump started running at 30 Hz (≈3000 kg/h). It was found that approximately 5 minutes was the timing for loading the slurry mixture before the cohesion of the particles would be to high and an immediate blockage of the system could be expected.

When the basis of heating was found approximately through experimental study, further investigation to understand the system was conducted with slurry mixtures. With all the pipes and most parts of the flow loop being thermally insulated, an experiment to find the possible thermally stable regimes were conducted. It was found that this flow loop connected with the chiller could be thermally stable at the lowest temperature of -3 °C, with the highest possible flow rate of 1700 kg/h. Also with this experiment, a basis with the above-mentioned pure liquids was first conducted and showed a lower thermally stable temperature.

After this basis were set, the following flow loop tests were performed following an established procedure. First, the chiller was set to -9°C, with the bypass line of the coolant liquid opened. Thereafter, the pre-cooled pure decane was charged into the loop, and the pump was started at 1600 kg/h. The pre-cooled pure decane cooled down the loop elements to negative temperatures, which prevented the initial melting of the ice particles. Next, the stirrer was activated, the flow was increased up to 2200 kg/h, and the concentrated ice slush was loaded to the top of the expansion tank. When the system was loaded with the particles, the bypass of the heat exchanger was gradually closed at a temperature read of -3°C in the tank volume, and the first sample for particle measurement was taken. When the temperature of the test section inlet and outlet reached the desired temperature for the experiment, the zero-time of the experiment was set and recording of pressure differences began. At this temperature, the flow rate was still 2000 kg/h This temperature was chosen as the lowest subcooling maintainable for a longer time (hours) in the rig and so achieve the highest possible cohesion between the particles *Yang et al.* (2004).

Afterward, the pressure drop measurements started at a slurry flow rate of 2000 kg/h. The duration of pressure drop measurements was limited to avoid the formation of significant deposits in the loop due to the slurry deposition. During each measurement, the flow was held constant for about three residence times of the system, and then the flow rate was reduced in seven stages down to the desired flow rate for the experiment.

3.1.2 Slurry preperation

For each experiment, a slurry mixture of decane (continuous phase) and ice particles (dispersed phase) had to be made to the set criteria for the experiment. The decane used for this study was supplied by the Sigma Aldrich company, with a chemical purity of >99%, and the ice particles were produced from in-house tap water, further shown in supplementary materials. From monthly reports on the quality of the water supplied

Table 3.2: Rheological expressions.

Reference	Expression
Thomas (1965)	$\mu_{mix} = \mu_l \cdot [1 + 2.5 \cdot \phi + 10.05 \cdot \phi^2 + 0.00273 \cdot exp(16.6 \cdot \phi)]$
Snabre and Mills (1996)	$\mu_{mix} = \mu_l \cdot (1-\phi) \cdot (1 - \phi/\phi_{\max})^{-2}$
Pabst (2004)	$\mu_{mix} = \mu_l \cdot (1-\phi)^{-2.5}$
Ford et al. (2006)	$\mu_{mix} = \begin{cases} \mu_a + \tau_y/\dot{\gamma} & \dot{\gamma} > \dot{\gamma}_0 \\ \mu_\infty & \dot{\gamma} \dot{\gamma}_0 \end{cases}$

from Svartediket around the city of Bergen, an average ph-degree of the water is to be expected around 8.0 ± 0.2. To produce the ice particles, water was collected in freezing trays and stored in a freezer at -22 ° C. When the water had completely frozen into ice cubes, the cubes were removed and crushed with decane in a blender (BN750EU from Ninja) into a mixture of the two phases. This mixture had a higher particle concentration than that of the desired for the experiments and was the last tank to be loaded after the piping and internal system were cooled down. For each step of crushing ice cubes, the weights were noted, so the desired concentration of slurry was obtained.

3.1.3 Rheological analysis

This section explains a part of the method for deriving a rheological analysis of the slurry. From *Yang et al.* (2004) the micromechanical measurement technique was conducted to compute the dynamic viscosity of the slurry within a known temperature regime. With this, the dependence of the slurry viscosity, μ_{mix}, on the particle concentration, ϕ, could be investigated. By testing various viscosity models against the flow loop measurements, the apparent viscosity of the slurry could be computed from pressure drop measurements. Table 3.2 presents the rheological expressions presented in the literature.

In Table 3.2, μ_l is viscosity of the continuous phase liquid, ϕ_{max} is the packing limit of the particles, τ_y is the yield stress, $\dot{\gamma}$ is the shear rate, μ_∞=80 Pa · s (*Ford et al.* (2006)) and $\dot{\gamma}_0 = \tau_y/(\mu_\infty - \mu_{mix})$ are the limiting viscosity and shear rate, μ_a is the apparent viscosity of the slurry from Thomas' model. The packing limit was calculated using the empirical expression by *Hoffmann and Finkers* (1995):

$$\phi_{\max} = (1 - [(1-0.416) \cdot \exp(-0.0142\rho d + \\ + 0.416)] \cdot \exp(-0.829\sigma)) \cdot \psi^{0.862} \quad (3.1)$$

where ψ is the mean circularity of the ice particles, σ is the geometrical standard deviation of the particle size distribution, d is the volume mean particle diameter in μm, and ρ is the particle density relative to the density of water.

The yield stress in Bingham's model (taken from *Ford et al.* (2006)) is given as (*Genovese* (2012)):

$$\tau_y = \sigma_s \cdot \left(\frac{2}{5\pi}\right) \cdot \left(\frac{\phi}{\phi_{\max}}\right)^{\frac{3}{3-fr}}, \tag{3.2}$$

where fr is the fractal dimension of particle agglomerates. In equation (3.2), $\sigma_s = F_c/d_0^2$ is the strength of an agglomerate consisting of primary particles with the size of d_0 (*Genovese* (2012)). The cohesive force for the ice particles in decane F_c can be found in the micromechanical measurements presented in *Yang et al.* (2004). For this calculation, an approximated experimental data set could be computed from *Yang et al.* (2004) by a polynomial using function *numpy.poly1d* in Python 3.8 (*Python* (2022)). The computed cohesive force using the polynomial for the cases within the experimental temperature interval *Yang et al.* (2004) could be computed. Finally, the shear rate γ could be computed using a system of equations for isotropic turbulence in a pipe flow, as presented in the literature *Flórez-Orrego et al.* (2012).

3.2 Particle size measurement

Measurement of the particle sizes was made both by optical measurement and digital. The optical measurement was done with the same sampling and investigation method over different slurry concentrations. At first, the slurry mixture was prepared in a small volume where several tests could be performed. The small sample was stored in the same freezer as the larger volumes of slurry used for experiments, where the freezer operated at temperatures of approximately $-22\ ^{\circ}C$. Equipment used for measurement was a cylindrical pipe with a diameter 2 mm, rigger-type paintbrush, black paper, 3d-printed pad, light source, and ruler. The ruler was cut and placed within the 3d-printed pad. A dry black paper was put on the 3d-printed pad, and all the equipment in use was put in the freezer for about 15 minutes to prevent high differential temperature between slurry and equipment. A schematic drawing of the set-up for particle photos is shown in figure 3.3

For each measurement, the slurry was taken out of the sample volume by vacuum transport with the cylindrical pipe. Two or three drops of the mixture was then placed on the black paper as close to the ruler as possible. The mixture were distributed evenly by brushing lightly with a paintbrush. The freezer top was then closed, and the pad with slurry and black paper was left inside for $\approx$15 min for the continuous phase (decane) to soak into the paper and the dispersed phase (ice particles) to be left clear on top of the paper.

Pictures of the particles were taken with the light source positioned opposite of the camera, directed on the pad with particles. The camera used for these photos was Leica Quad Camera (20 MP, f/2.2, 16 mm). Processing of the images was done in the ImageJ-software, where the method was the same for each measurement. At first, the

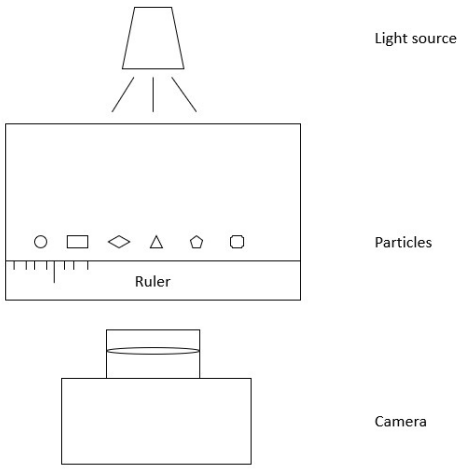

Figure 3.3: Model of the set-up made for photoes of the particles taken from slurry.

scale was transformed from pixels to a known distance in mm, defined by the ruler. The image was then cropped to remove the ruler, and transformed into an 8-bit image to differentiate between particles in brighter colours, and the black paper of darker color. In further processing a band-pass filter, with particle filter 3-40 pixels, with a 5 % tolerance direction. The image was then processed with the sharpen function two times for easier detection of edges, and finally, the area of each particle was measured by drawing around each particle and then selecting Analyze-Measure. The results were transferred to excel, where the diameter of each particle was calculated by assuming spherical particles from the equation.

3.3 Particle drop-tests

For investigating the coefficient of restitution in ice-particle collisions, an experimental model to determine the forces in the collision was to be built. The main idea is that this model would be able to trace particle movement in a drop test, where a water droplet will be submerged in sub-cooled decane. The first method for testing was that the spherical particle consisting of tap water would freeze after dropping through a tube before hitting a smooth ice surface with the desired angle. For this, a theoretical calculation of the time needed for freezing was calculated. From the calculations, desired lengths of the tubing for this model were found for different temperature ranges of the continuous phase liquid decane. In the research, the temperature ranges were set to -5, -15, and -20 ° C, and the corresponding critical distance for achieving a shell thickness of 0.002401 m/m considering a volume of 70 μl water droplet was found to 1.26, 0.34 and 0.23 m for the temperature ranges previously mentioned, respectively. Both settling with a constant terminal velocity and with acceleration weere computed.

From the theoretical calculations, a transparent glass tubing (borosilicate glass 3.3) with a length of 36 cm and an inner diameter 30 mm was picked to achieve the critical length for the conditions of -15 and -20 ° C. At the bottom of the horizontal pipe,

a smooth ice surface at 45° was placed, accompanied by a vertical and horizontal ruler expansion to determine the velocity and bounce of the particle. A schematic representation of the model is shown in figure 3.4.

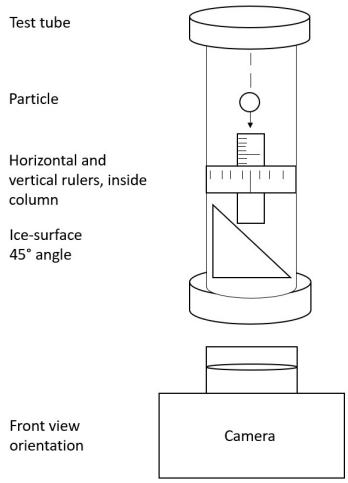

Figure 3.4: Schematic model of the model for drop test experiments.

A table of full results regarding the critical length and settling time for critical shell thickness of the particle surface from the equations computed is shown in supplementary materials. The terminal velocity found in equations of a particle droplet of 70 μl was calculated to $v_T = 0.223$ m/s when dropped in subcooled decane to a temperature -20°C.

From the figure shown in 3.4, the particle drop-tests were conducted. The procedure for this measuring included two phases; first, the particles were produced, secondly, the particles were dropped onto the ice surface as depicted in the model. The first testing of this measurement model was done as intended, where a water droplet of volume 70 μl was dropped in a glass tube piping from a pipet, where the liquid was subcooled to -20°C. The result of this method became not so convenient for later research, as the spherical ice-particles could agglomerate, divide into two droplets or either break on impact or during the last stages of freezing to the core as the expansion forces broke the particles. With this method, the water was pushed out at a constant rate from the pipet with full expansion of the lever containing the liquid.

The solution to this problem was dividing the experiment into two phases, first producing the ice spheres during the drop test in a taller horizontal pipe, where an additional 15 cm stainless steel 304 pipes was connected to the glass tubing of 36 cm while subcooling the water by leaving the tip of the pipet with the liquid in the decane for approximately 5 seconds before the water was pushed out at a slower rate than previous of the pipet. This resulted in a higher success rate of forming spherical ice particles without breaking, agglomeration, or dividing. A total of nine particles were made for the final particle drop tests.

During the drop tests, the model was changed and an additional guide tube was inserted, to help guide the dropping of the particles to the desired area, so terminal velocity and the velocity after a collision could be determined more frequently. The particle's movement was recorded in a slow-mo regime, and the time between frames was computed. The velocities of the particles were determined by screenshots, where the video was processed in a Windows media player and the frames were manually changed to a set amount, of which the corresponding time could be determined. The screenshots were further processed in the free online version of PlotDigitizer-software. In this program the photos could be uploaded, the reference lengths were set by the ruler in the set-up, and a point could be set at the middle of the particle in question, of which the program provided the coordinates in xy-directions. The coordinates were later transferred to an Excel sheet, where the frames between the particles were converted to time change, and the difference in coordinates over time resulted in the velocity of the particle. The particles did not fall in a straight vertical line, as impurities in the surface of the particle, or movement when dropping gives the particle a horizontal velocity of which particle movement when falling through the pipe will differ.

Later the effects of the guide tube were investigated by comparing the absolute velocities of the particles with and without this tube inserted. The falling of the particles was also investigated over a set of temperatures in the liquid. A picture of the spherical droplets was taken with the set-up shown in the particle measurements method, to determine the circularity of the particles. The particles were processed with the same procedure as for particle measurements of the slurry mixture.

Chapter 4

Results and Discussion

This chapter presents the findings of the experimental method explained in chapter 3. The main parts involved in the results are particle size measurements, flow loop experiments, and particle drop tests.

4.1 Overview of experiments

In this study, the pressure readings and particle sizes have been recorded of the flow loop system through a series of experiments where parameters like the flow rate, particle concentration, and the temperature have been changed to develop control of the flow loop system. The testing of the flow loop is divided into two phases, where the first series spans from August-December 2021, where a total of 30 experiments were recorded differentiating the flow rate from 330-1700 kg/h, the temperature from -4 to -1°C, and particle concentrations from 0-20.3%. Based on the experimental data from the first series, models of blockage risk evaluation were applied, further described in later parts. For the second series, the goal was to obtain a blockage at the orifice in a well-known flow regime to further investigate particle interactions with the radioactive particle and PEPT-tracing.

The second series spans from January-April 2022, where a total of 18 experiments were recorded. For these experiments, the free space at T-junctions was removed, further reducing the depositions at these parts in the flow loop. For this series plugs were not induced at the orifice, but the flow assurance was improved. The most intensive deposition was at -1 °C and 400 kg/h with slurry volume concentrations of 5-10 %. The system was investigated with a set of parameters, particle concentration %volume of three values, 5-10-15, flow rates of three sets with long term experiments for 400-900-1400 kg/h, and a set of two temperatures -1°C and -2°C.

Table 4.1: Plug experiments, series 2 temperature -1 °C.

Concentration, % vol.	Flow rate, kg/h		
...	400	900	1400
5	OPB	NB	LPB
10	LB	LPB	NB
15	LB	LPB	NB

Table 4.2: Plug experiments, series 2 temperature -2 °C.

Concentration, % vol.	Flow rate, kg/h		
...	400	900	1400
5	LB	NB	LPB
10	LPB	NB	NB
15	NB	LPB	NB

An overview of the experiments conducted in series 2 is shown in table 4.1 and 4.2, where NB= no blockage, LPB= loop partial blockage, OPB= orfice partial blockage and LB= loop blockage.

4.2 Flow loop pressure drop readings

The differential pressure drops were measured for slurries with volume fraction up to 20.3 % both at the orifice- test section and over the entire loop, where the total pressure was between the pressure recorded after the pump ("P") to the pressure in the expansion tank. As seen in the literature, the pressure drops is expected to rise with an increasing flow rate following a power-law type. In figure 4.1 the total pressure drop in the flow loop system is shown for different slurry volume concentrations, as a function of flow rate. For a better graphical representation, the data was processed in Origin software.

From experimental data, the pressure drop over the orifice test section of pure continuous phase liquid (decane) was 0.010 bar at 400 kg/h (Re= 4956), and 0.330 bar for the same phase at a flow rate of 2000 kg/h (Re=24778). In the slurry mixture of 20.3 volume % concentration for the same flow rates the pressure over the orifice test section the pressure drop was 0.015 bar and 0.331 bar. This indicates that the pressure drop varies differently when the slurry volume concentration increases, in percentage, 400 kg/h = 50 % higher, and 2000 kg/h = 0.3 % higher pressure drops. For the total pressure drop, a similar result is obtained, where pure decane was equal to 0.124 bar for 400 kg/h and 1.09 bar for 2000 kg/h. For the slurry mixture (20.3%) the total pressure drop was 0.179 and 1.147 bar for the flow rates, which resulted in 44.4 % and 5.2 % higher pressure drops, respectively. These results are as expected in the literature where *Beata Niezgoda-Zelasko* (2007), *Onokoko et al.* (2018) and *Bordet et al.* (2018) obtained similar results.

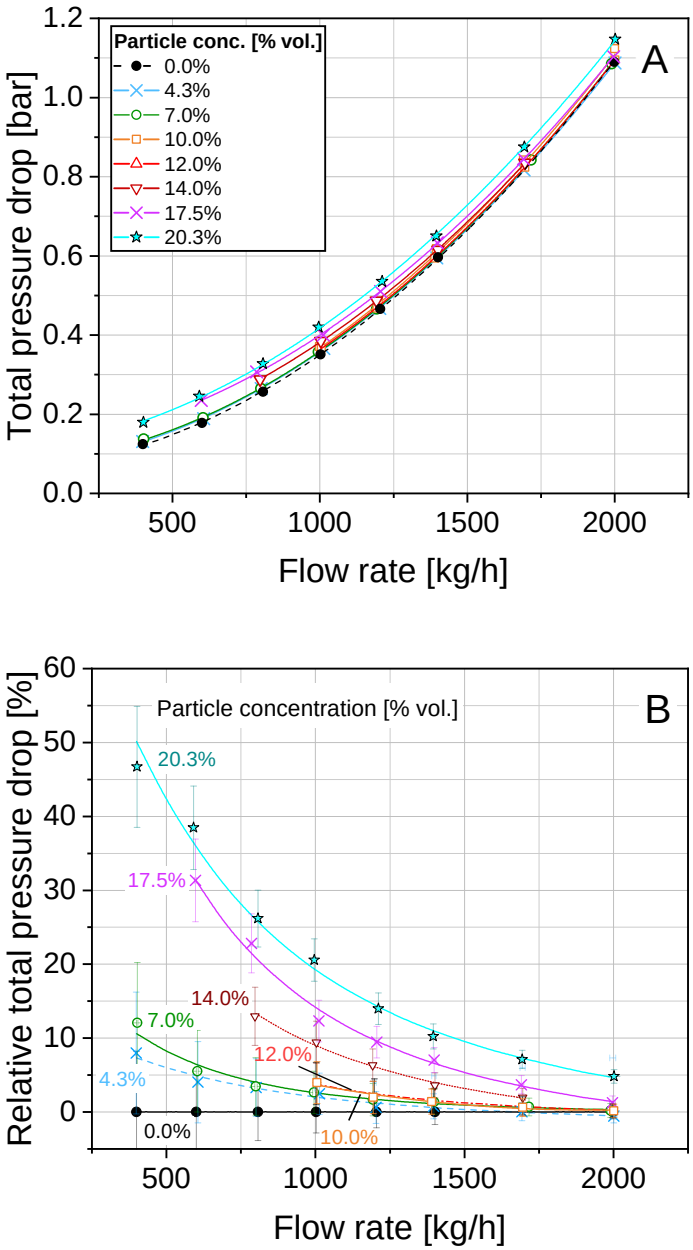

Figure 4.1: Absolute (A) and relative (B) total pressure drop in the ice slurry flow (between "P" pressure sensor and the expansion tank).

This effect is a cause of enhanced energy dissipation, further caused by particle-wall interactions and inter-particle collision. In the flow loop experiments, it was observed that particle deposits appear near the inner surface of the flow loop piping, and the rate of deposition was dependent on the flow conditions where a lower flow rate increased deposition, resulting in a significant increase in total pressure drop for flow rates lower than 1000 kg/h.

The slurry viscosity was later estimated by fitting the pressure drop from equation 2.5, to the experimental data with the least-square fitting technique. The data was collected in an Excel file, the result can be seen in figure 4.2. For these calculations the local Reynolds number was computed from $Re_{i/j} = \rho_{mix} u_{i/j} d_{i/j} / \mu_{mix}$.

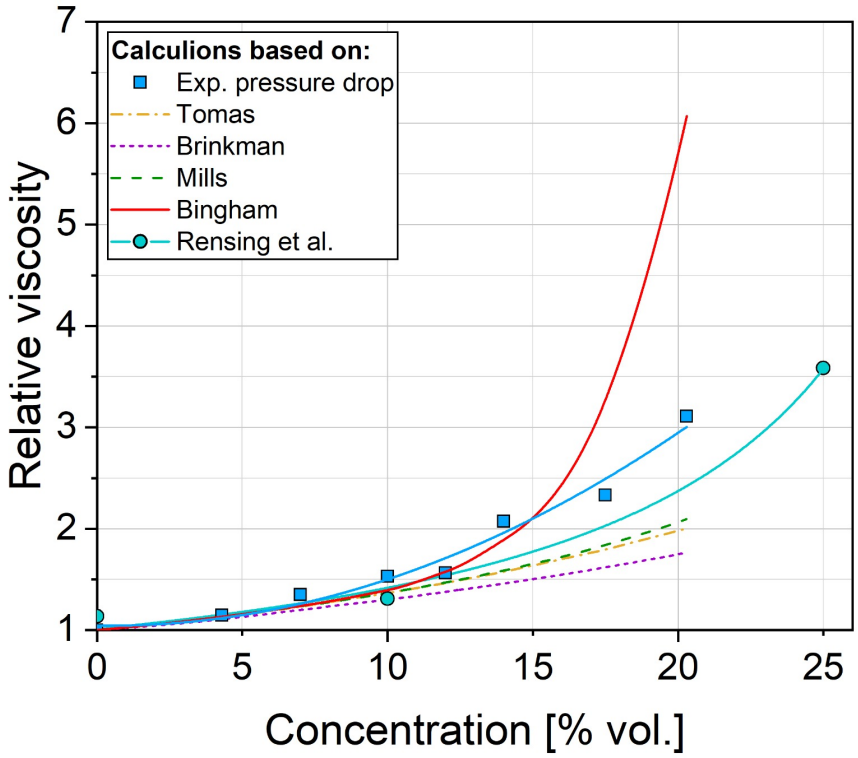

Figure 4.2: Relative viscosity of ice slurry.

The relative viscosity μ_{mix}/μ_l is presented in the figure for different slurry volume concentrations. The figure shows the behavior of relative viscosity with slurry volume concentration, reaching a value of 3.0 for 20.3 volume % concentration, for pressure drop over the orifice. It is also apparent in the figure that the relative viscosity behavior is more noticeable for concentrations above 12 %.

For validation, experimental results from *Rensing et al.* (2011) for a similar oil-based slurry is also shown in the figure. The discrepancy of a lower viscosity in experiments to the data from Rensing is explained by the temperature regime, where temperature control of -1°C, increases the cohesion between the particles, resulting in a higher relative viscosity.

Models from Thomas, Brinkman, and Mills show an agreement of the data up to 12 % slurry volume concentration, where the average discrepancies at ϕ<12% for Thomas, Brinkman, and Mills models are 6.75 %, 4.57 %, and 3.76 %, respectively. For denser slurries (ϕ>12%) it can be seen a higher degree of mismatch, where discrepancies up to 58.5 % are obtained (Brinkmann). The models when comparing themselves also show discrepancies, but for the experimental data presented, it is concluded that the rheological models are not accurate for the dense slurry, explained by the deviation from the homogeneous flow condition.

The data is more acceptable comparing to the *Rensing et al.* (2011) and Bingham's model (*Ford et al.* (2006)), when averaged over the experimental interval of flow rate variation. When the particle concentration exceeds 12 %, a rapid growth of relative viscosity computed from the Bingham-fluid model is shown, and the experimental data seems to have a relation between the experimental data from *Rensing et al.* (2011) and this model. The average discrepancy for particle concentration (ϕ>12%) is 35 % and 22 % for the Bingham and Rensing models respectively.

4.2.1 Flow map- risk evaluator

For achieving a system control of the flow loop system, experiments with the intention of plug formation at the orifice in the test section were conducted. The orifice was inserted, as plug formation is related to local flow restrictions, i.e. where the piping is partially obstructed. Several cases of blockage were achieved.

A study of mapping the plugs were then conducted, where the most traditional approach is based on flow morphology maps. The main parameters of the multiphase flow for this purpose are the Reynolds number and slurry volume concentration *Peker and Helvac* (2008); *Ramsdell and Miedema* (2013). In *Doron and Barnea* (1996), a flow map including the flow regimes of homogeneous flow, moving bed, stationary bed, and a formation where plug formation is possible is presented. *Hirochi et al.* (2002) also presents a flow map based on experimental results.

Another approach is conducted by *Chaudhari et al.* (2018), where the possibility of plugging is presented in a risk-based map. This map involves the gas-emulsion flow laden with hydrates, where the emulsion was formed by water droplets dispersed in an oil phase. With a dimensional analysis, this blocking risk evaluator was proposed:

$$BRE_h = 500 \frac{\phi / (1-\phi) LL}{[Re\,(1-LL)]^{0.52} Ca^{0.27}}, \tag{4.1}$$

where ϕ is the volume fraction of particles, Re is the Reynolds number, LL is the volume fraction of emulsion, and Ca is the capillary number responsible for the solid phase cohesion due to liquid bridges.

With the only continuous phase liquid in the slurry mixture in our case being decane, the equation is adopted. The standard capillary number is defined as granular capillary number Ca_g=$\mu_l u/\gamma_c$, where u is an average flow velocity, and $\gamma_c = 4F_c/3\pi d_0$ the interfacial energy per unit area of ice in decane. The experimental data from Yang et al.*Yang et al.* (2004) is then fitted into the equation, then $2F_c/d_0 \sim$1.4 N/m for ice in decane at -1^0 C is obtained. The liquid loading is equal to 1, as there is no gas in the system, and making use of the Taylor series expansion, an asymptotic value of the risk evaluator is derived by *Struchalin* (2022):

$$BRE = \lim_{LL \to 1} BRE_h = 1042 \frac{\phi/(1-\phi)}{Re^{0.52} Ca_g^{0.27}}. \tag{4.2}$$

The risk evaluator map was made out of cases where a plug were formed in the flow loop system at an earlier stage in the experiments. For all experiments, the loading method was of the same procedure as mentioned in chapter 3. The experiments parameters is shown in table 4.2.1, OB = Orifice Blockage, OFP= Orifice partial blockage, LB = Loop blockage:

experiment	1	2	3	4	5	6
Initial flow rate [kg/h]	1500	400	400	700	500	400
slurry vol. concentration [%]	2.2	6.8	6.9	7.1	7.2	7.2
blockage timing	4hrs 18min	2 minutes	1hr	5 minutes	12 min	8 min
Type blockage	OB	LB	LB	OB	LB	LB

In experiment nr 1, the orifice was blocked over a long time, where the deposit gradually increased. In other experiments, a slug could be seen entering the flow, most likely detached from some geometrical obstruction inside the pipe system.

With the experimental data obtained from the experiments, the risk evaluator- map was then produced. The risk evaluator is shown in figure 4.3:

In figure 4.3, the grey zone of the diagram, the risk for blocking is imminent and increases towards the middle of the area. From the diagram it can be seen that the slurry mixture of 7% volume concentration is within the grey area, and from experimental results, blockages were obtained for these concentrations. The initial flow rate describes the flow rate which was set after the loading, meaning that for all cases, the flow rate was changed from ≈2000 kg/h to the initial flow rate. In this instance, all experiments conducted with 7 % volume concentration moved through the grey area of the risk evaluator, and the blockage was to be expected. From optical observations of the experiments, the flow loop was as mentioned plugged as a result of a large piston-like deposition clogging the flow.

The risk evaluator seems to be comparable with experimental results, however, the long-term experiment with a 2.2 % volume concentration slurry would not result in a blockage when considering the risk evaluator, but an orifice blockage was obtained for this experiment. For this experiment a partial blockage was first obtained at the orifice in the first hour of the experiment, the flow rate then gradually decreased to 500 kg/h 3.9 hours into the experiment. The deposit was later, 3:48 hours, into the experiment partially re-suspended by the flow. The result was that the flow rate increased to 600 kg/h, then the full blockage of the cross-section occurred. The experiment was researched thoroughly, and the conclusion for the deviation of a blockage occurring

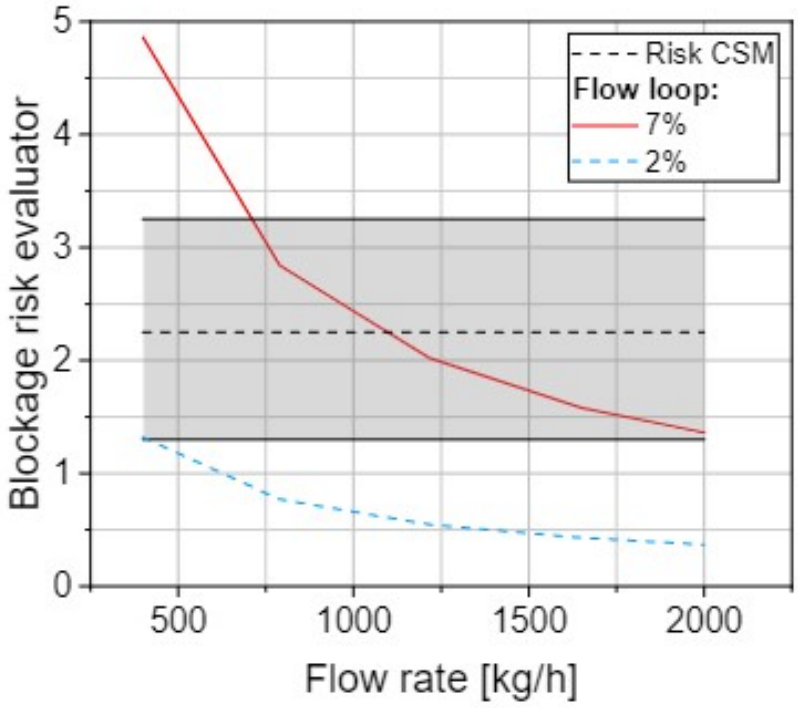

Figure 4.3: Blockage risk evaluator.

outside the area depicted in the risk evaluator was concluded as the formation of particulate deposits before the orifice, their partial re-suspension to the flow and the respective formation of particulate slugs. In other words, the re-suspension of flow rate altered the particulate flow in the system, resulting in a higher chance of plugging.

4.2.2 Summary

In the flow loop experiments, the differential pressure drop curve was found in a mixture of 75 wt% water and 25 wt % ethanol mixture. The total pressure drop as a function of flow rate was measured for different slurries of particle volume concentration 4.3 - 20.3 % and compared to a pure liquid decane. Further, a graphical representation of the relative viscosity of the same set of slurry mixtures is compared to other models obtained in the literature, with a comparable result for ϕ<12% . For denser slurry volume concentrations the discrepancy grew up to 58 %, and it was concluded that the rheological expressions were not accurate for dense slurries, explained by the deviation of homogeneous flow.

A flow map was introduced as a risk evaluator adapted from the approach by *Chaudhari et al.* (2018), where the experimental data set was of blockage induced experiments of different sets of parameters shown in table 4.2.1. The risk evaluator could correctly predict the plugs formed in the flow loop system.

4.3 Particle size distributions from the samples

This section represents the result of particle size measurements. This part includes the measurement of particle sizes and circularity of the produced photos taken from slurry sampling. First, comparison of the manual method of detecting the edges of each particle to the automatic particle analyzing method in Image-J software is shown. Thereafter the results of particle measurement taken from the flow loop are shown. Further measurements taken from the flow loop during the conducting of a set experiment is shown and how run time influence the mean average particle size. In the last part, the change in mean average particle size and circularity is presented in comparison.

4.3.1 Manual count of particles

After the method of collecting slurry and processing the data as explained in 3 was conducted, the first particle measurement could be determined, and it was decided to do this manually. In the manual method, an amount of 100 particles were measured, with a mean particle diameter size of ($D_p = 0.53$ mm). This was done manually at the time as it was seen as the most accurate reading, where the edges of the particles could easily be determined, by zooming the photo to a small area. This method required a lot of time for obtaining the results, and a more suitable method was of interest. The Image-J software also applied an automatic analysis function for area measurement, where the only difference is the program deciding the edges of the particles as a difference of grey value. The question was then if the newly found method gave the same results as the previous, and a comparison of the methods was conducted. In this stage of the experiments, the circularity of the particles, was not of interest yet, as the main focus was to compare the methods for particle sizes. The methods were conducted on the same photo, and a frequency distribution graph of the particle size for both methods was obtained. This experiment was conducted on a slurry mixture batch volume, of particle volume concentration 7%, which was kept in a freezer subcooled to -20°C. The image of the particles is shown in figure 4.4.

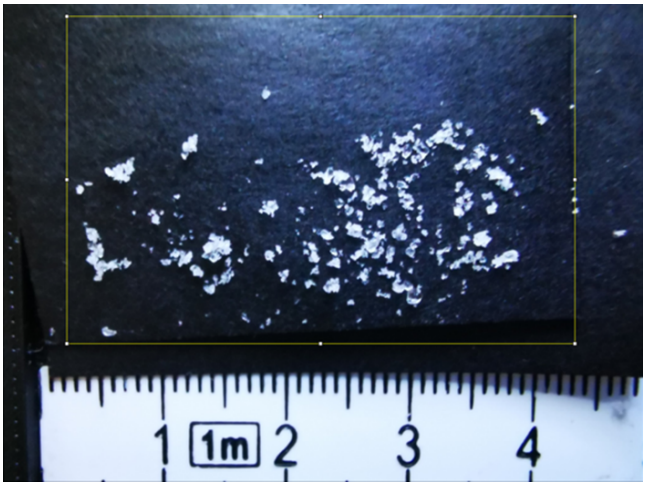

Figure 4.4: Ice particles.

The image was then processed, and the result is shown in figure 4.5.

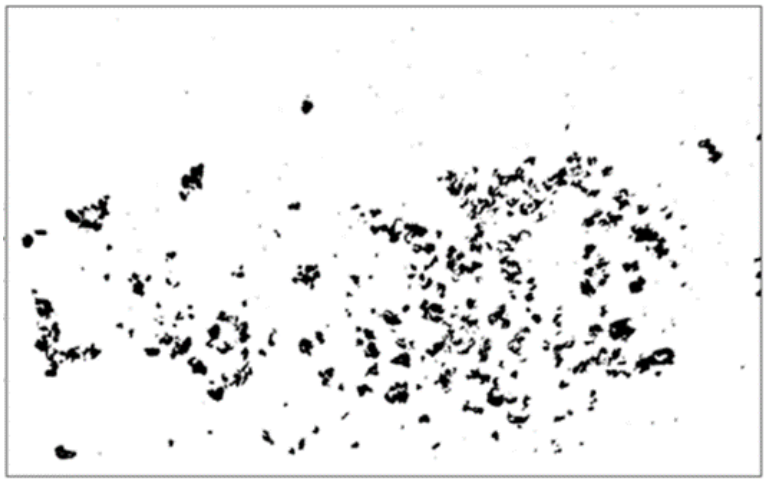

Figure 4.5: Projected area of particles.

From the automatic analysis, the outlines the program determined can be shown, with manual analysis this is not possible, as a drawing of the measurement area had to be set for each measurement. The outlines from the automatic analysis are shown in figure 4.6.

In the manual method, the area of a total of 164 particles was measured. The area was then recalculated into particle diameter by the formula of a sphere ($D_p = \sqrt{\frac{4A}{\pi}}$). In the automatic analysis of the photo, the program detected 169 particles. The frequency distributions for the two methods are shown in figure 4.7.

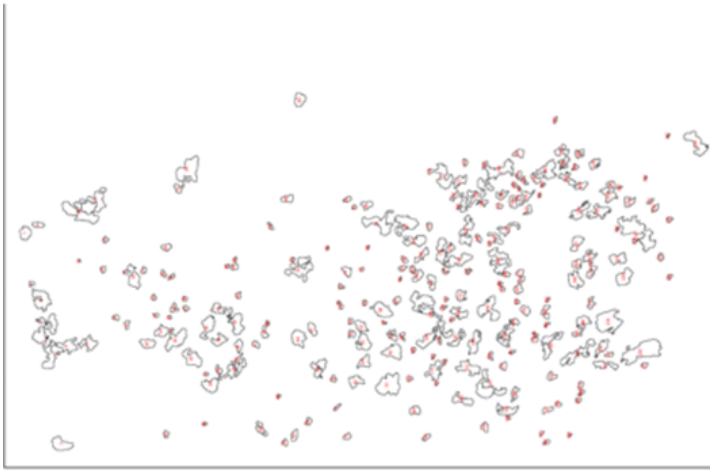

Figure 4.6: Outlines of particles.

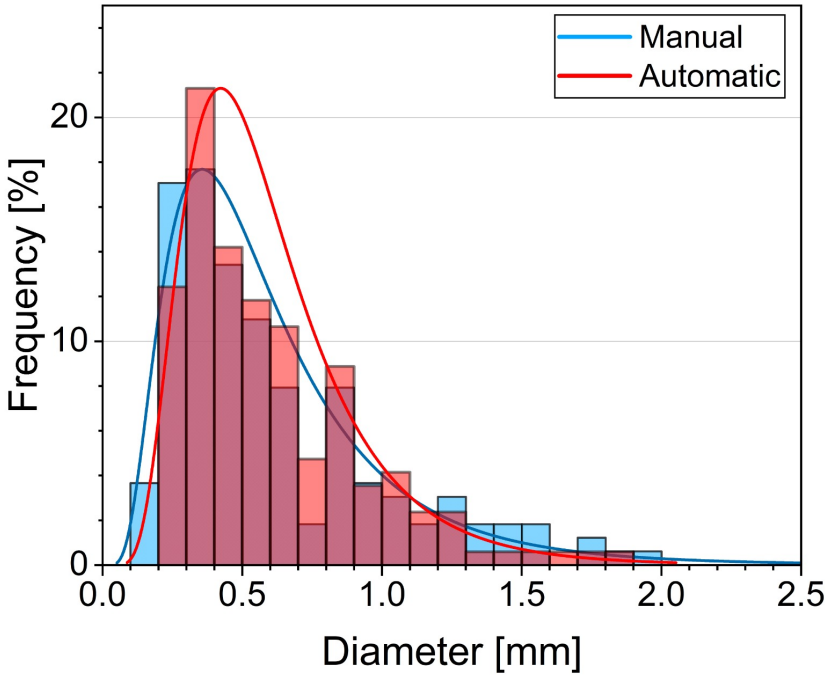

Figure 4.7: Frequency distribution of particle size's compared.

Comparing the results from the manual area measurement and automatic area measurement in figure 4.7, the similarities are clear. In both cases the amount of particles start at a lower amount before reaching its maximum, both at a particle diameter size of 0.3-0.4 mm, and further declining towards the maximum set value, indicating tendencies of a log-normal distribution. This is to be expected, as the particle size diameter often is presented in log-normal distributions in the literature, and is useful for further calculating the packing factor of the slurry mixture *Hoffmann and Finkers* (1995). If a log-normal approach is determined in these graphs, the single-mode would be at 0.41 mm, with a standard deviation of 0.39 mm. In both graphs, there is a spike in the range of 0.8-0.9 mm particle diameter size.

The first discrepancy is in the number of particles in the two methods, where in the manual measurement a total of 164 particles were detected and measured, as compared to 169 particles in the automatic measurement. One reason for this can be seen when comparing the photos of the particles. Comparing figure 4.4, 4.5 and 4.6, while focusing on the largest particle in the middle-left part of the photos, it can be seen as a large agglomerate in the original photo, but after processing as a cluster of particles with a hole in the middle. As shown in figure 4.6, the program detects two particles in this part, as the manual method would look at the original photo while drawing the outlines on the processed photos, and determine this as one particle. However, the question if this is just one particle is unclear, as a small hole in the same particle can be seen in the original photo, but not sufficient enough to divide the particle into multiple parts.

Another problem is the lack of particles measured with a particle diameter of the range between 0.1-0.2 mm, where the manual method detected a total of six particles within this range. The reason for this is thought to be when drawing the edges manually, the drawing is not smooth, but follows a pixelated path. The stability and patience of the researcher will also have an effect, where a twitching of the arm can influence the edge drawing at a higher amount when considering a smaller area. This will not be a problem with the automatic method, as the edges are determined by the grey values of the two values 0 and 255, indicating black or white respectively. The automatic method, therefore, determines the pixel of the processed photo by these values to either detect a particle or not.

In table 4.3.1, the average, maximum and minimum particle size diameters are presented for the measurements. The average diameter of the batch volume for both methods is shown to be $\approx$0.6 mm. The "uncertainty" of both maximum and minimum values is $\pm$0.1 mm, comparing the manual method to the automatic, where the manual method shows both the highest maximum and lowest minimum particle diameter size.

	Manual method	Automatic method
Average diameter [mm]	0.613	0.605
max	1.910	1.808
min	0.1554	0.2547

For further investigations, the circularity of the particles became an interesting factor. This measurement was found to be highly dependant on the quality of the photo, focus contributing as the main contributor. The circularity measurement was also applied by the Image-J software, before measuring the area it had to be chosen as a wanted result. Circularity measurements of the manual method of area measurement were not done.

4.3.2 Average diameter and circularity

It was further investigated if the average particle diameter sizes, and the circularity where dependent upon the volume concentration of the slurry mixture. The volume concentrations chosen where 5, 10 and 15 % volume concentration of the dispersed phase in the slurry mixture. The result is presented in table 4.3.2.

volume concentration %	Average diameter [mm]	Average circularity
5	0.44	0.35
10	0.46	0.30
15	0.30	0.39

Comparing these values to previously shown values in table 4.3.1, it can be seen that the average particle diameter size has decreased, this is thought to be due to changing of the mixer, as there was a crack in the first mixer, and a new one was bought. All other methods for preparing the slurry, and processing the photos was conducted as previously, and this is the only parameter that changed. It can be seen in table 4.3.2 that the highest volume % concentration of slurry (15%), has a lower average particle diameter then that of the two other concentrations. Further experiments were conducted, and it was found that the average D_p could vary anywhere in between from 0.30-0.60 for all slurry concentrations. The average circularity was as previously mentioned highly dependent on the quality of the photo, but average values of 0.2-0.7 was most often found, and the average of the average circularity span was set to a value of 0.525.

4.3.3 Change in diameter through flow loop experiments

To see the changes in the particle diameter in the flow loop, long-term (over 6 hours) experiments were performed, where sampling of the slurry was taken in intervals. For the selected experiment, a 4% volume concentration of the slurry mixture was selected. In this experiment, the particle diameter size distribution was determined at the start of the experiment when the flow rate was still 2000 kg/h, throughout the experiment at different intervals, and at the end of the experiment when the flow loop had been blocked.

flow rate [kg/h] run time [min]	Average diameter [mm]	Average circularity
2000 0	0.42	0.48
1500 10	0.45	0.25
1500 30	0.39	0.37
1500 60	0.38	0.20
1320 90	0.37	0.35
0 110	0.36	0.40

The result shown in table 4.3.3, shows a declining trend of the average D_p through flow loop experiments. This suggests that either the larger particles settle in the flow loop as deposition, or are crushed during the flow loop experiment. From this experiment where a loop blockage was recorded, it is highly likely that for this case the larger particles deposited in the system, and this resulted in plugging.

The next step was to investigate the change of D_p and circularity in the flow loop system, after the geometrical shape was changed. For this, experiments conducted in the second series of experiments, without free space at T-junctions was the basis. In these experiments, the flow rate was set to 400 kg/h after loading, and the system was held thermally stable for as long as possible before the flow loop system experienced a blockage or the system was shut down. Another parameter that can be investigated in this section is the change according to plug-induced incidents, as in these experiments, plug formation was achieved. Sampling of these experiments was performed at the start of the experiment, when the flow rate was 2000 kg/h, and at the end when the flow loop was blocked or stopped. For these experiments, the temperature was kept at -2°C and -1°C, for the same concentrations as previously investigated in "average diameter and circularity" section. All sampling was taken from the tank top of the flow loop system and stored in the freezer to prevent heating of the slurry. The results are compared for the different volume concentrations and shown in figure 4.8.

Concentrating on the 5 % volume concentration slurry mixture, there was a partial blockage of the orifice for the experiment where the temperature of the test section was held thermally stable at -1°C. In the other case, where the temperature across the test section was held thermally stable at -2°C, a loop blockage of the system was obtained. For both cases, the average D_p increased towards the end of the experiment. The factors of change were 1.61 and 1.36 with the largest change for the temperature regime of -2°C.

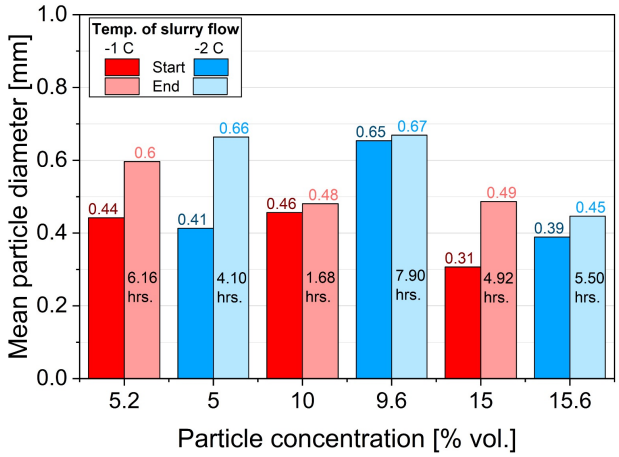

Figure 4.8: Average D_p of volume concentration slurry mixtures.

Concentrating on the 10 % volume concentration slurry mixtures, the graph shows a small increase in D_p towards the end of the experiment, with a factor of >1.1 for both temperature regimes, and is not considered large enough to have had any effect on the system. A loop blockage was experienced for the case of temperature regime -1°C, and only a partial loop blockage for the latter.

The highest slurry concentration mixture, 15 %, also had an increase in D_p, where the temperature regime of -1°C had the most significant change with a factor of 1.6, compared to 1.15 for the temperature regime of -2°C. In the latter case, it was not possible to obtain a blockage of the system, as the flow loop operated for several hours, only a small deposition around the orifice was seen, and it was deemed to stop.

Comparisons of the circularity was also investigated, and is shown in figure 4.9.

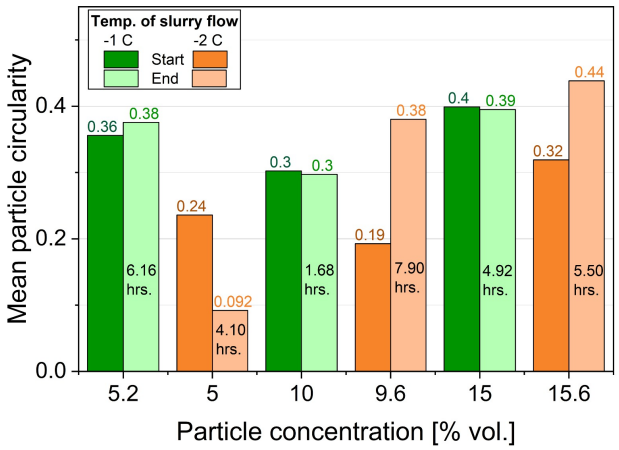

Figure 4.9: Average circularity of volume concentration slurry mixtures.

Concentrating on the 5 % volume concentration slurry mixture, the graph shows two contradicting trends, where the temperature regime of -1°C shows a small increase (factor <1.1) in the circularity of the particles, and the other case shows a significant decrease with a factor of >2.5. Since the circularity is highly dependent on the quality of the photo, the accuracy of this measurement is questionable.

With further investigations of the circularity changes, it can be seen that all cases with a thermally stable system of -1°C have the same trend, where the factor of increase/decrease is deemed stable, as it is <1.0. However, for the thermally stable regime of -2°C, the factor of change is a lot more dominant. Comparing the 10 and 15 % volume concentration slurry mixtures to the 5 % as previously mentioned, the result is once again contradicting, where the factor of change now becomes positive, with factors of 2 and 1.375 for 10 and 15 % mixtures respectively. This can be a result of lower cohesion between the particles, where particle interactions will shape the particles, rather than agglomerate together.

4.3.4 Ice particle's properties

With the investigation of particle measurement coming to a full, a review of the ice particles in itself is presented. From figure 4.4, the characteristic ice particle appearance is shown. The shape of the ice particles is irregular, and the fractal dimension, as well as packing factor was found by following the method described in chapter 3, rheological analysis, by combining the rheological expressions from table 3.2, with the equations of packing limit from equation 3.1 (*Hoffmann and Finkers* (1995)), and the yield stress in Bingham's model 3.2, taken from (*Ford et al.* (2006)). From this, the fractal dimension of the ice particles was found to be 2.57 and resulted in a packing limit of ice powder of $\phi_{max} = 0.56$, which is close to the packing limit found in the works of *Hirochi et al.* (2002) for an ice-water slurry.

4.3.5 Summary

The mean particle size (D_p) of the dispersed phase (ice particles) was investigated over a set of parameters (changing during flow loop experiments, relation to volume concentration of slurry mixture, relation to plug induced incidents). It was found that the particle size range is between 0.2 to 2.1 mm, and if considered a log-normal size distribution the single mode is 0.41mm and a standard deviation of 0.39 mm. The average circularity of the particles is perhaps the most uncertain in this experiment, as the value was highly dependent of the quality on the photo. From a fresh slurry mixture with a good quality on the photo, the average circularity measurement showed higher values, and the circularity of one of these photos, not presented in the report, was the basis for determining the average circularity of ice particles to 0.525.

For the cases studying change in particle diameter through flow loop experiments, a declining average particle diameter is present and could be explained by partial melting in regions with a positive local temperature, or the sampling method itself, so the largest particles deposit before they left the stream. In further experiments when the sampling was taken from the tank top during plug-inducing incidents, the average D_p was found to slightly increase for most cases. The packing limit of the ice powder could then be determined by following a rheological analysis presented in the literature 3.1. The fractal dimension of the particles was 2.57, and the packing limit of the ice powder was $\phi_{max} = 0.56$, which resembled the values found in *Hirochi et al.* (2002).

4.4 Particle drop test velocities

Most of the results obtained from particle drop tests were computed in Excel. For the preliminary results, eight ice droplets were made by the method described in chapter 3, and kept in a subcooled decane volume set to a temperature of -20 °C. A picture of the particles was taken following the method of particle measurements for ice slurry, to evaluate the spherical conditions of these droplets.

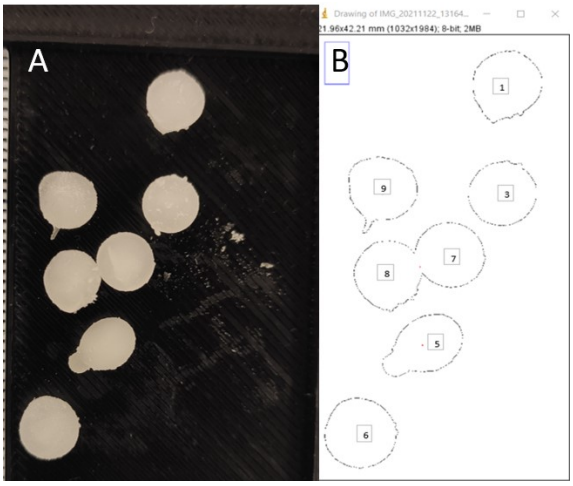

Figure 4.10: Particles (A), and projected area (B).

The average values of the particles diameter and circularity is presented in table 4.4.

	Average diameter [mm]	Average circularity
Average	6.1	0.820
maximum	6.0	0.726
maximum	6.4	0.915

After this, the drop testing began, and the terminal velocity was determined as the absolute velocity of the particles in the drop test. Theoretical values operate with a perfect sphere, of which absolute velocity during drop testing will become the terminal velocity of the particle in the y-direction. In practical experiments, this is as previously mentioned not possible, and the absolute velocity, $v_{abs} = \sqrt{(v_x)^2 + (v_y)^2}$, was compared to the terminal velocity in theoretical values, instead of the velocity in the y-direction.

In the drop test experiments, the total average absolute velocity was 12.01 cm/s, and there was no clear indication of bounce when the particles hit the ice surface, and it was decided that the rolling velocity down the ice surface of 45° was to be investigated. The method included the same as for determining the absolute velocity of the particle drops, with the zero frames chosen as the frame of collision between ice-particle-ice-surface.

For this case, the total average rolling velocity was 6.05 cm/s. The next part of the experiments was to investigate if a guide tube could help the experiment, as a higher chance of success with rolling velocity measurements would be possible. A feasibility study comparing the dropping of the particles in three temperature regimes was conducted, where the temperatures chosen were -5, -10 and -15 °C. The result of this study is shown in figure 4.11 and figure 4.12 for absolute and rolling velocity, respectively.

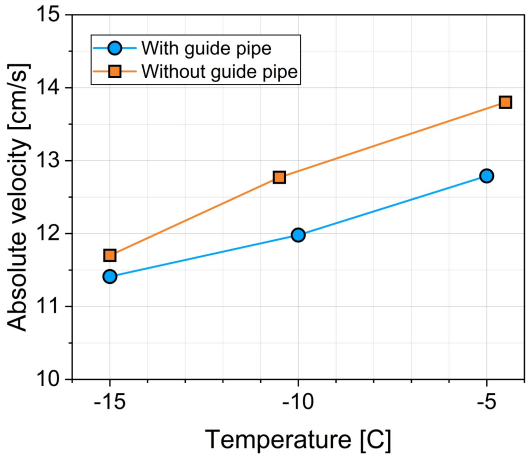

Figure 4.11: Absolute velocity.

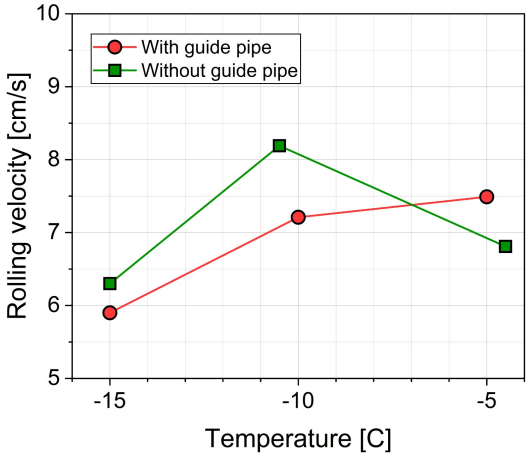

Figure 4.12: Rolling velocity

In the graphs, it is clear that the guide tube decreased the absolute and rolling velocity of the particles, with a discrepancy in the results of rolling velocity for temperature regime -5 °C. The total averages with recovery coefficient are shown in table 4.4 and table 4.4 for inserted guide tube and system without guide tube, respectively.

Temperature [°c]	-15	-10	-5
Absolute velocity	11.41	11.98	12.79
Rolling velocity	5.9	7.21	7.47
Recovery coefficient	0.517	0.602	0.584

Temperature [°c]	-15	-10	-5
Absolute velocity	11.7	12.77	13.8
Rolling velocity	6.3	8.19	6.81
Recovery coefficient	0.538	0.641	0.493

From this result, it was clear that the influence of the guide pipe was an undesired factor, and all experiments were conducted without the guide tube, with a smaller chance of success for measuring rolling velocities.

When comparing the obtained velocities to the theoretical, the experimental results show lower values of a factor of 1.83 for the absolute experimental velocity to the theoretical terminal velocity. The difference in temperature in the medium is also clear in the experimental results, and the influence of the guide pipe is found to be of a higher degree in the medium of higher temperatures. The rolling velocities are also shown to increases with the decreasing temperature, except for the case of temperature regime -5 °C, where the cohesion of the ice surfaces increase as expected from the literature.

In further experiments, this set-up was meant to investigate the collisions further by dropping a radioactive water droplet and tracing the droplet with a PET scanner at the University Hospital of North Norway in Tromsø, but this part of the experiments was delayed and later stopped due to various unpredictable incidents.

Chapter 5

Conclusions and future work

5.1 Conclusion

This thesis presents flow loop data for the slurry flow of ice in decane. A broad range of volume slurry concentrations, different temperature regimes, and flow rates were investigated for inducing a plug in the flow loop system. The objective was to measure the pressure drop in the system as well as over the orifice in the test section, to derive a dimensionless control to determine flow loop plugging. The particle size diameters, circularity, and concentration were investigated through the flow loop run time. The sampling of the flow was done throughout the flow loop experiments, where the samples at the start and end of the experiment were processed for average diameter particle sizes and circularity. The volume fraction of particles was below 20 %, and the Reynolds number was in the range from 5000 to 25000.

During experiments, it was found that the pressure drop in the slurry was most sensitive to the presence of particles when the Reynolds number was below 1000. With the pressure drop data, the apparent viscosity of the flow was estimated and showed similarities to a Bingham type fluid, shear-thinning tendencies. The computed viscosity was higher than the values predicted by rheological expressions. The viscosity was higher because of the formation of particulate deposits in the flow loop and the reduction of the cross-section of the pipe, at the test section. The orifice imposed a flow resistance in the loop, which increased the possibility of plugging the flow loop system.

Several cases of plugging where studied for volume slurry concentrations of 2.2 and 7 %. For the 7 % volume slurry concentration, plug formation was often observed within a relatively short flow loop run time of several minutes. In the experiments it was observed that the flow regime had a slug-like tendency, where large agglomerates of the dispersed phase (ice) collided with the front surface of the orifice. When large slugs collided with the front of the orifice, a rapid growth of a deposit was initiated that blocked the orifice. With smaller volume concentrations of slurry, the deposit gradually formed at the orifice at lower rates. A stationary layer of particles was also observed to form at the bottom of the horizontal pipe, growing in the upstream direction.

To forecast the plugging events, a risk evaluator was adopted to determine the plug formation dimensionless. The risk evaluator was adopted from the Colorado School of Mines, and is also present in literature, currently in press. The risk evaluator was found to accurately predict plugging.

5.2 PEPT-experiments for particle tracking

To further understand the dynamics behind flow loop plugging, the particle forces must be investigated. The ice-particle-ice-surface interactions can further be used to investigate the the forces acting on each particle, when approaching the orifice in a flow loop experiment. The particle movement can be traced across the orifice, and the forces acting on the particle when encountering the flow resistance can be investigated.

Bibliography

Baha Abulnaga, P. (2021), *Slurry systems handbook*, McGraw-Hill Education. (document), 2.2.1, 2.4

Beata Niezgoda-Zelasko, J. (2007), Generalized non-newtonian flow of ice-slurry, *Chemical Engineering and Processing - Process Intensification*, *46*, 895–904, doi:10.1016/j.cep.2007.06.008. 2.1, 4.2

Bordet, A., S. Poncet, M. Poirier, and N. Galanis (2018), Flow visualizations and pressure drop measurements of isothermal ice slurry pipe flows, *Experimental Thermal and Fluid Science*, *99*, 595–604, doi:10.1016/j.expthermflusci.2018.04.024. 2.1, 4.2

Chaudhari, P., L. E. Zerpa, and A. K. Sum (2018), A correlation to quantify hydrate plugging risk in oil and gas production pipelines based on hydrate transportability parameters, *Journal of Natural Gas Science and Engineering*, *58*, 152–161, doi:10.1016/j.jngse.2018.08.008. 4.2.1, 4.2.2

Crowe, S. J. S. M. . T. Y., C.T. (), *Multiphase Flows With Droplets And Particles (2nd ed.)*. (document), 2.2.1, 2.2.1, 2.3, 2.2.3, 2.2.4

Darbouret, M., M. Cournil, and J.-M. Herri (2005), Rheological study of tbab hydrate slurries as secondary two-phase refrigerants, *International Journal of Refrigeration*, *28*(5), 663–671, doi:10.1016/j.ijrefrig.2005.01.002. 2.1

Ding, L., B. Shi, Y. Liu, S. Song, W. Wang, H. Wu, and J. Gong (2019), Rheology of natural gas hydrate slurry: Effect of hydrate agglomeration and deposition, *Fuel*, *239*, 126–137, doi:10.1016/j.fuel.2018.10.110. 2.1

Doron, P., and D. Barnea (1996), Flow pattern maps for solid-liquid flow in pipes, *International Journal of Multiphase Flow*, *22*(2), 273–283, doi:10.1016/0301-9322(95)00071-2. 4.2.1

encyclopedia, B. (2022), Archimedes' principle, https://www.britannica.com/science/Archimedes-principle, Online; accessed 10-May-2022. 2.2

Fidel-Dufour, A., F. Gruy, and J.-M. Herri (2006), Rheology of methane hydrate slurries during their crystallization in a water in dodecane emulsion under flowing, *Chemical Engineering Science*, *61*(2), 505–515, doi:10.1016/j.ces.2005.07.001. 2.1

Flórez-Orrego, D., W. Arias, D. López, and H. Velásquez (2012), Experimental and cfd study of a single phase cone-shaped helical coiled heat exchanger: an empirical correlation, in *Proceedings of the 25th international conference on efficiency, cost,*

optimization, simulation and environmental impact of energy systems, pp. 375–394. 3.1.3

Ford, C., F. Ein-Mozaffari, C. Bennington, and F. Taghipour (2006), Simulation of mixing dynamics in agitated pulp stock chests using cfd, *AIChE journal*, *52*(10), 3562–3569, doi:10.1002/aic.10958. 3.2, 3.1.3, 3.1.3, 4.2, 4.3.4

Geest, C. v. d., A. Melchuna, L. Bizarre, A. C. Bannwart, and V. C. Guersoni (2021), Critical review on wax deposition in single-phase flow, *Fuel*, *293*, 120,358, doi:doi.org/10.1016/j.fuel.2021.120358. 1.1

Genovese, D. B. (2012), Shear rheology of hard-sphere, dispersed, and aggregated suspensions, and filler-matrix composites, *Advances in colloid and interface science*, *171*, 1–16, doi:10.1016/j.cis.2011.12.005. 3.1.3, 3.1.3

Hirochi, T., S. Yamada, T. Shintate, and M. Shirakashi (2002), Ice/water slurry blocking phenomenon at a tube orifice, *Annals of the New York Academy of Sciences*, *972*(1), 171–176, doi:10.1111/j.1749-6632.2002.tb04569.x. 1.1, 2.1, 3.1.1, 4.2.1, 4.3.4, 4.3.5

Hoffmann, A., and H. Finkers (1995), A relation for the void fraction of randomly packed particle beds, *Powder Technology*, *82*(2), 197–203, doi:10.1016/0032-5910(94)02910-G. 3.1.3, 4.3.1, 4.3.4

Idelchik, I. E. (2008), *Handbook of Hydraulic Resistance, 4th Edition Revised and Augmented*, Begell House, Inc. 2.2.2, 5.2.1, 5.2.1, 5.2.1

Majid, A. A., W. Lee, V. Srivastava, L. Chen, P. Warrier, G. Grasso, P. Vijayamohan, P. Chaudhari, E. D. Sloan, C. A. Koh, et al. (2018), Experimental investigation of gas-hydrate formation and particle transportability in fully and partially dispersed multiphase-flow systems using a high-pressure flow loop, *SPE Journal*, *23*(03), 937–951, doi:10.2118/187952-pa. 2.1

Onokoko, L., M. Poirier, N. Galanis, and S. Poncet (2018), Experimental and numerical investigation of isothermal ice slurry flow, *International Journal of Thermal Sciences*, *126*, 82–95, doi:10.1016/j.ijthermalsci.2017.12.017. 2.1, 4.2

Pabst, W. (2004), Fundamental considerations on suspension rheology, *CERAMICS SILIKATY.*, *48*(1), 6–13. 3.2

Peker, S. M., and S. S. Helvac (2008), *Solid-Liquid Two Phase Flow*, Elsevier, doi:10.1016/B978-0-444-52237-5.X5001-2. 4.2.1

Poloski, A., M. Bonebrake, A. Casella, M. Johnson, P. MacFarlan, J. Toth, H. Adkins, J. Chun, K. Denslow, M. Luna, and J. Tingey (2009), *Deposition Velocities of Non-Newtonian Slurries in Pipelines: Complex Simulant Testing*, vol. PNNL-18316 WTP-RPT-189 Rev. 0. 2.2.1

Python (2022), numpy.poly1d, https://numpy.org/doc/stable/reference/generated/numpy.poly1d.html, [Online; accessed 31-March-2022]. 3.1.3

Ramsdell, R. C., and S. A. Miedema (2013), An overview of flow regimes describing slurry transport, in *Proceedings WODCON XX - Congress and Exhibition: The Art of Dredging*. 4.2.1

Rensing, P. J., M. W. Liberatore, A. K. Sum, C. A. Koh, and E. D. Sloan (2011), Viscosity and yield stresses of ice slurries formed in water-in-oil emulsions, *Journal of Non-Newtonian Fluid Mechanics*, *166*(14-15), 859–866, doi:10.1016/j.jnnfm.2011.05.003. 2.1, 4.2

Sloan, E. D. (2010), *Natural gas hydrates in flow assurance*, Gulf Professional Publishing, doi:10.1016/C2009-0-62311-4. 1.1

Snabre, P., and P. Mills (1996), I. rheology of weakly flocculated suspensions of rigid particles, *Journal de Physique III*, *6*(12), 1811–1834, doi:10.1051/jp3:1996215. 2.1, 3.2

Struchalin, V. H. K. P. H. A. C. B. B. V., Pavel G. (2022), Flow loop study of a cold and cohesive slurry. pressure drop and formation of plugs., In press. 4.2.1

Thomas, D. G. (1965), Transport characteristics of suspension: Viii. a note on the viscosity of newtonian suspensions of uniform spherical particles, *Journal of colloid science*, *20*(3), 267–277, doi:10.1016/0095-8522(65)90016-4. 3.2

Vijayamohan, P., A. Majid, P. Chaudhari, E. D. Sloan, A. K. Sum, C. A. Koh, E. Dellacase, and M. Volk (2014), Hydrate modeling & flow loop experiments for water continuous & partially dispersed systems, in *Offshore Technology Conference*, OnePetro. 2.1

Yang, S.-o., D. M. Kleehammer, Z. Huo, E. D. Sloan, and K. T. Miller (2004), Temperature dependence of particle–particle adherence forces in ice and clathrate hydrates, *Journal of colloid and interface science*, *277*(2), 335–341, doi:10.1016/j.jcis.2004.04.049. 3.1.1, 3.1.1, 3.1.3, 3.1.3, 4.2.1

Supplementary materials

5.2.1 Computing viscosity from the pressure drop data

The viscosity of the liquid can be determined using the pressure drop over the part of the hydraulic system. In this case, the total pressure drop ΔP is the sum of the pressure drops ΔP_i at the individual sections of the system. The individual pressure drop is given as (5.1):

$$\Delta P_i = \xi_i \frac{\rho_l u_i^2}{2}, \tag{5.1}$$

where $\xi_i = f(Re)$ is the coefficient of hydraulic resistance for a specific section (straight pipe, bend, tee e.t.c), ρ_l and u_i are the density and the velocity of the liquid. The Reynolds number is computed as (5.2):

$$Re_i = \frac{\rho_l u_i d_i}{\mu_l}. \tag{5.2}$$

Here d is the hydrodynamic diameter of the hydraulic section, and μ_l is the viscosity.

The viscosity of the slurry is determined by iterating over the pressure drop calculations till the condition $\Delta P_{exp} = \Delta P_{calc}$ is true. The equations for determining the pressure drops at local sections of the loop are taken from Idelchik's handbook *Idelchik* (2008). Below we omit the indices "i", meaning that the equations presented are used for each section of the hydraulic system individually, using the flow rates, Reynolds numbers, and associated coefficients determined for this section.

Pressure drop in the pipes
The pressure drop in the pipes is determined as (5.3):

$$\Delta P_p = \lambda \frac{l}{d} \frac{\rho_l u^2}{2}, \tag{5.3}$$

where λ is the Darcy friction factor, and l is the pipe length.

The friction coefficient of the pipe is given as (5.4):

$$\lambda = \begin{cases} 0.11 \cdot \left(\frac{\Delta}{d} + \frac{68}{Re}\right)^{0.25} & Re > Re_2, \\ \left[(\lambda_2 - \lambda^*) \cdot exp\left[-[0.0017(Re_2 - Re)]^2\right] + \lambda^*\right] & Re_1 < Re < Re_2, \\ 4.4 \cdot Re^{-0.595} \cdot exp\left(\frac{-0.00275d}{\Delta}\right) & Re < Re_1, \end{cases} \tag{5.4}$$

where Δ is the mean roughness of the pipe surface (taken equal to 50 μm),

$$Re_1 = 1160\frac{d}{\Delta}, \tag{5.5}$$

$$Re_2 = 2090 \cdot \left(\frac{d}{\Delta}\right)^{0.0635}, \tag{5.6}$$

$$Re_2 = 2090 \cdot \left(\frac{d}{\Delta}\right)^{0.0635}. \tag{5.7}$$

Re_1 is determined in Eq.(5.5) when $\Delta/d > 0.007$.
In Eq.(5.4), the coefficients λ_2 and λ^* are defined as in Eq.(5.8) and Eq.(5.9):

$$\lambda_2 = \begin{cases} 7.244 \cdot Re_2^{-0.643} & \Delta/d0.007, \\ \frac{0.145}{\left(\frac{\Delta}{d}\right)^{-0.244}} & \Delta/d > 0.007, \end{cases} \tag{5.8}$$

$$\lambda^* = \begin{cases} 0.032 & \Delta/d0.007, \\ 0.0758 - \frac{0.0109}{\left(\frac{\Delta}{d}\right)^{0.286}} & \Delta/d > 0.007. \end{cases} \tag{5.9}$$

There are 3.2 m of 22-mm and 0.2 m of 35-mm straight pipes in the flow loop.

Pressure drop in the bends

The loop has ten 90° bends of 22-mm pipes, and two 45° bends of 35-mm pipes. The pressure drop in the bends is determined as (5.10):

$$\Delta P_{bend} = \xi_{bend} \frac{\rho_l u^2}{2}, \tag{5.10}$$

where ξ_{bend} is the coefficient of the local hydraulic resistance and, defined in Eq.(5.11):

$$\xi_{bend} = \begin{cases} \frac{A}{Re} + \xi_{loc} + 0.0175\delta\lambda\frac{R}{d} & 3\cdot 10^3 < Re < 10^4, \\ k_\Delta k_{Re}\xi_{loc} + 0.0175\delta\lambda\frac{R}{d} & Re 10^4. \end{cases} \tag{5.11}$$

In Eq.(5.11) R is the major radius of the bend (equal to the inner diameter of the pipes), δ is the angle of the bend in degrees. The coefficient λ, ξ_{loc}, and k_{Re} are determined by in Eq.(5.4), (5.12), and (5.13), correspondingly. The coefficients A and k_Δ are determined by diagram 6.1 in *Idelchik* (2008). The ratio R/d equals unity for six bends are placed outside of the test section and equal to 2 for the bends of the test section.

$$\xi_{loc} = 0.21 \left(\frac{R}{d}\right)^{-0.5}, \tag{5.12}$$

$$k_{Re} = 1.3 - 0.29 \cdot ln\left(Re \cdot 10^{-5}\right) \tag{5.13}$$

Pressure drop in the flowmeter

The internal pipes of the flowmeter have a flattened U-shape. Based on the computer tomography of the flowmeter, and the technical data, we determined the dimensions of the pipes. The pressure drop in the flowmeter is determined using Eq.(5.1), where the coefficient ξ_{fm} is given as (5.14):

$$\xi_{fm} = 2\xi_{90fm} + \lambda \frac{l_{fm}}{d_{fm}}, \tag{5.14}$$

$$\xi_{90fm} = \lambda \cdot \left(\frac{l_{fm}}{d} + 0.035 \cdot 90 \cdot \frac{R_{fm}}{d_{fm}} \right) + A_1 \cdot \xi_{sb}, \tag{5.15}$$

$$\xi_{sb} = 0.0175 \cdot 90 \cdot \lambda_{el} \cdot \frac{R_{fm}}{d_{fm}}. \tag{5.16}$$

Here λ is defined as for the straight pipe (Eq.(5.4)), R_{fm} and d_{fm} are the bend radius (40 mm) and the diameter of the flowmeter pipe (8.8 mm), λ_{el} is determined in diagram 6.2 in *Idelchik* (2008), and is taken $A_1 = 1.51$ based on recommendation in diagram 6.18 in *Idelchik* (2008). The ratio R/d is taken equal to 4.5 for this case.

Pressure drop in the flexible hose

The flow loop contains a curved flexible hose with inner diameter of 20 mm. The pressure drop in the flexible hose had been calculated according Eq.(5.1) with the coefficient of hydraulic resistance ξ_{fh} determined in Eq.(5.15) with $A_1 = 2$. The coefficient $\lambda_e l$ required for calculation ξ_{sb} was from diagram 6.2 in *Idelchik* (2008). The ratio R/d here is equal to 9.

Pressure drop in T-junctions

The set-up contains several types of T-junctions (T): a T dividing and uniting the flow (Ts of the injection section), a flow-turning blind-T with a dead end, and a straight T where a branch is plugged. The pressure drop there is given by Eq.(5.1), while the coefficients ξ_i were determined by summarizing the recommendations in diagrams 7.1 - 7.31 in *Idelchik* (2008). They are presented in Table 5.1, depending on the type of the tee.

Tee type	ξ_i
Dividing the flow	1.075
Uniting the flows	0.688
Blind-T	1
Straight T	0.13

Table 5.1: The values of ξ_i for different types of T-junctions.

Pressure drop in expansions and restrictions of the cross-section

The set-up contains several expansions and restrictions of the cross-section. The pressure drop is calculated using Eq.(5.1). The coefficient ξ_i depends on the type and geometry of an expansion or a restriction.

The coefficient $\xi_{pipe-fm}$ of the transition from the loop pipe to the flowmeter is given as (5.17):

$$\xi_{pipe-fm} = \begin{cases} 0.5 & Re < 10^4, \\ 0.5 \cdot \left(1 - \frac{F_0}{F_1}\right)^{0.75} & Re 10^4, \end{cases} \tag{5.17}$$

where F_0 and F_1 are the cross-section areas of the flow meter‘s pipes and 22-mm loop pipe, correspondingly. In Eq.(5.17), the Reynolds number is based on the flow velocity in the pipes of the flow meter.

The transition from the flow meter to the flexible hose is an expansion and its coefficient of hydraulic resistance ξ_{fm-fh} is defined as (5.18):

$$\xi_{fm-fh} = \left(1 - \frac{F_0}{F_2}\right)^2. \tag{5.18}$$

In Eq.(5.18), F_2 is the cross-section area of the flexible hose.

The flexible hose contains two pressed adaptors with an inner diameter of 16 mm at its ends. The adaptors create both the restrictions and expansions of the flow area. Their total contribution to the pressure drop of the flow is defined by Eq.(5.1) for each of the two expansions and restrictions, using Eq.(5.17) and Eq.(5.18) for the determination of the local coefficients of the hydraulic resistance. In this case, the variable F_0 means the cross-section area of the narrow pipe (16 mm), and the variables F_1 must be replaced by F_2, which here is a wide channel (20 mm).

The coefficient $\xi_{fh-tank}$ of the transition from the flexible hose to the expansion tank is equal to unity, and the velocity of the flow is being taken as for the flexible hose.

5.2.2 Particle drop test

Settling with a constant terminal velocity																		
Temperature, C	-20						-15						-5					
Volume, L*10^(-6)	5	10	15	30	50	70	5	10	15	30	50	70	5	10	15	30	50	70
Terminal velocity, m/s	0.1029	0.1271	0.1434	0.175431	0.203153	0.223465	0.1029	0.1271	0.1434	0.175431	0.203153	0.223465	0.1029	0.1271	0.1434	0.175431	0.203153	0.223465
Critical distance, m	0.0531	0.0787	0.0986	0.144169	0.190572	0.229035	0.0757	0.1140	0.1441	0.2134	0.284175	0.342884	0.2115	0.3440	0.4546	0.725179	1.01616	1.264853
Critical time, s	0.5161	0.6189	0.6872	0.8218	0.93807	1.024925	0.7357	0.8969	1.0046	1.216435	1.39882	1.5344	2.0564	2.7063	3.1702	4.133705	5.001945	5.66019
Shell thickness (part of the radius), m/m	0.0011	0.0014	0.0015	0.001885	0.002183	0.002401	0.0011	0.0014	0.0015	0.001885	0.002183	0.002401	0.0011	0.0014	0.0015	0.001885	0.002183	0.002401
Heat transfer coefficient, W/(m2·K),	1534	1492	1469	1429.197	1401.638	1383.713	1534	1492	1469	1429.197	1401.638	1383.713	1534	1492	1469	1429.197	1401.638	1383.713

Settling with aceleration (v0 = 0)																		
Temperature, C	-20						-15						-5					
Volume, L*10^(-6)	5	10	15	30	50	70	5	10	15	30	50	70	5	10	15	30	50	70
Terminal velocity, m/s	0.1029	0.1271	0.1434	0.175431	0.203153	0.223465	0.1029	0.1271	0.1434	0.175431	0.203153	0.223465	0.1029	0.1271	0.1434	0.175431	0.203153	0.223465
Critical distance, m	0.0515	0.0763	0.0956	0.139834	0.184789	0.222068	0.0741	0.1116	0.1411	0.209027	0.27832	0.335826	0.2100	0.3416	0.4516	0.720874	1.010196	1.257656
Critical time, s	0.5331	0.6402	0.7114	0.85112	0.97237	1.06265	0.7525	0.9181	1.0285	1.245335	1.432765	1.571715	2.0728	2.7272	3.1938	4.161525	5.035345	5.696885
Shell thickness (part of the radius), m/m	0.0011	0.0014	0.0015	0.001885	0.002183	0.002401	0.0011	0.0014	0.0015	0.001885	0.002183	0.002401	0.0011	0.0014	0.0015	0.001885	0.002183	0.002401

*Buoyancy added

Figure 5.1: Settling time velocities of ice particles dropped in subcooled decane.

5.2.3 Water quality

Telefon, avdeling Vannforsyning: 55 56 75 00
Besøksadresse, avdeling Vannforsyning: Spelhaugen 22, 5147 Fyllingsdalen
Telefon, Bergen Vann: 55 56 60 00
Epost Bergen Vann: Bergenvann@bergen.kommune.no
MVA/Organisasjonsnummer: 964 338 531

Kvalitet på vann levert fra Svartediket vannbehandlingsanlegg i 2021

Svartediket forsyner normalt sett til Bergen sentrum
Det forsyner også vestre deler av Bergen sammen med Espeland,
og områdene Kokstad, Hjellestad/Milde og Skjold/Nordås sammen med Kismul og Espeland.

Analyseresultat fra rentvann ved Svartediket vannbehandlingsanlegg i perioden 1.1.2021 – 31.12.2021
Analysene er utført ved Bergen Vann sitt Vannlaboratorium og Eurofins
Prøvegruppe, grenseverdi/tiltaksgrense er oppgitt ihht. krav i drikkevannsforskriften
https://lovdata.no/dokument/SF/forskrift/2016-12-22-1868
AFA= "akseptabel for abonnentene", IUE= "ingen unormal endring"

Parameter	Prøvegruppe	Enhet	Snitt	Maks	Min	Antall	Grenseverdi/ tiltaksgrense
1,2-dikloretan	B	µg/l	0,38	0,38	0,38	3	3
Aluminium	A	mg/l	26,0	35,0	20,0	3	200
Ammonium	B	µg/l	16,667	25,000	12,500	3	500
Antimon	B	µg/l Sb	0,040	0,050	0,033	3	5
Arsen	B	µg/l	0,03	0,03	0,03	3	10
Benzen	B	µg/l C6H6	0,100	0,100	0,100	3	1
Benzo(a)pyren	B	µg/l	0,00	0,00	0,00	3	0,01
Bly	B	µg/l	0	0	0	3	10
Bor	B	µg/l	15	15	15	3	1000
Bromat	B	µg/l BrO3-	2,50	2,50	2,50	3	10
Clostridium perfringens	B	ant/100 ml	0,00	0,00	0,00	2	0
Cyanid	B	µg/l	1,00	1,00	1,00	3	50
E.coli	A	ant/100 ml	0,000	0,000	0,000	51	0
Farge	A	mg/l Pt	2,5	13,0	2,0	51	AFA/IUE
Fluorid	B	mg/l	0,150	0,150	0,150	3	1,5
Intestinale enterokokker	A	ant/100 ml	0,00	0,00	0,00	51	0
Jern	B	mg/l	9,412	27,000	1,000	51	200
Kadmium	B	µg/l	0,01	0,01	0,01	3	5
Kimtall	A	ant/ml	6,48	300,00	0,00	50	100 og IUE
Klorid	B	mg/l	6,067	6,800	5,400	3	250
Koliforme bakterier	A	ant/100 ml	0,00	0,00	0,00	51	0
Ledn.evne	A	mS/m, 20°	12,0	13,2	10,8	52	250
Kobber	B	mg/l	0,2	0,2	0,2	3	2000
Krom	B	µg/l	0,030	0,055	0,010	3	50
Kvikksølv	B	µg/l	0,00	0,00	0,00	3	1
Lukt	A	Sensorisk	0,76	1,00	0,00	51	AFA/IUE
Mangan	B	µg/l	5,23	9,10	2,50	3	50
Natrium	B	mg/l	3,13	3,40	2,90	3	200
Nikkel	B	µg/l	0,53	0,62	0,47	3	20
Nitrat	B	µg/	0,099	0,120	0,085	3	50
Nitritt	B	µg/l	5,000	5,000	5,000	3	500
Selen	B	µg/l	0,025	0,025	0,025	3	10
Smak	A	Sensorisk	0,780	1,000	0,000	50	AFA/IUE
Sulfat	B	mg/l	7,533	8,200	6,700	3	250
PAH 4 ***	B	µg/l	0,006	0,006	0,006	3	0,1
Trihalometaner total	B	µg/l	0,350	0,350	0,350	3	100
pH	A	pH	8,060	8,300	7,700	52	6,5-9,5
Tetrakloreten	B	µg/l	0,100	0,100	0,100	3	10
TOC	B	mg/l	1,7462	3,4000	1,3000	13	IUE
Turbiditet	A	NTU	0,11	0,17	0,05	52	AFA/IUE
Trikloreten	B	µg/l	0,05	0,05	0,05	3	10

Figure 5.2: Chemical composition water.